École polytechnique de Louvain

Numerical investigation of sheet flow sediment transport

Author: **Loïk Pierson**
Supervisors: **Vincent Legat, Jonathan Lambrechts**
Readers: **Michel Henry, Matthieu Constant, Paul Fisette**
Academic year 2024–2025
Master [120] in Electro-mechanical Engineering

Acknowledgments

I would like to express my sincere gratitude to my supervisors, Prof. Vincent Legat and Prof. Jonathan Lambrechts, for their guidance and support throughout this thesis. I am particularly grateful to Michel Henry for his invaluable help at every stage, and for his constant availability in answering my questions and assisting with the code.

Contents

1 Introduction

1.1 Goal of this work

The goal of this work is to apply the immersed granular numerical model of `migflow`, see Constant et al. [Con+19] and Henry et al. [Hen+25], to the study of sediment transport. More specifically, we will focus on the sheet flow regime, which is an intense bed load transport regime that occurs both in natural environments such as rivers and coastal areas, and in industrial processes such as dredging and mining. The scope of this work will be limited to 2D flume-like experiments to assess the model's ability to reproduce at least qualitatively the phenomenon. The scaling behavior of sheet flow will also be investigated in the same conditions.

To achieve this, a review of the physics involved is presented in section 1.2. A classical analytical description of the fluid phase is made in section 1.2.1 and section 1.2.2 then a modest description of the physics of sediment transport and sheet flow is presented in section 1.3. In section 2 we describe and parametrise the numerical experiments, of which the results are presented in section 3. A number of tools had to be developed around `migflow` specific to the problem and will be presented along with the results.

1.2 Inclined flows

1.2.1 Laminar fluid flow over an inclined plane

In rivers, sediment transport occurs in inclined open channels. However, to be able to reproduce a variety of sediment transport experiments setups from the literature, we will not limit ourselves to open channels. To simplify the problem and work in two dimensions, we will assume the open channel flow can be approximated as a flow over an inclined infinite plane with constant depth and thus an unresolved free surface. The closed channel flow will be approximated by a flow between two parallel and infinite planes. For the analytical computations, we will further simplify the fluid problem to 1D. As the boundary condition for an unresolved free surface is a simple symmetry condition, both cases can be treated in the same way, considering the open channel depth as half of the closed channel width. We will see later that to sweep through the higher transport regimes without exploding the computation time nor getting silly unphysical domains, we will need to add a driving force in addition to the bed slope. As such, we will generalise by including a pressure gradient term in the x direction, which is normally impossible for a uniform open channel flow. Equivalently, we will allow ourselves to impose a body force in the flow direction. We thus consider a steady, two-dimensional, fully developed flow of water over an inclined plane, with constant flow depth along the streamwise direction. We will first assume the flow to be laminar, and then extend the analysis to turbulent flow.

The momentum equations in the x- and y-directions for an incompressible fluid are given by:

$$\rho\left(\frac{\partial u}{\partial t}+u\frac{\partial u}{\partial x}+v\frac{\partial u}{\partial y}\right)=-\frac{\partial p}{\partial x}+\mu\left(\frac{\partial^2 u}{\partial x^2}+\frac{\partial^2 u}{\partial y^2}\right)+\rho F_x \tag{1}$$

$$\rho\left(\frac{\partial v}{\partial t}+u\frac{\partial v}{\partial x}+v\frac{\partial v}{\partial y}\right)=-\frac{\partial p}{\partial y}+\mu\left(\frac{\partial^2 v}{\partial x^2}+\frac{\partial^2 v}{\partial y^2}\right)+\rho F_y \tag{2}$$

Where the body force $F[ms^{-2}]$ contains the gravity vector tilted with respect to the reference frame and the user-defined body force in the flow direction (x) :

$$F_x = g\sin\theta + f_x \tag{3}$$
$$F_y = -g\cos\theta + f_y = -g\cos\theta \tag{4}$$

Assumptions

1. **Incompressible fluid**: The density ρ of the fluid is constant and the divergence of the velocity $\nabla \cdot \mathbf{v}$ is null.
2. **Uniform flow**: in the context of open-channel flows, the depth of a uniform flow is constant, and thus the domain is a rectangle.
3. **Steady flow**:
$$\frac{\partial u}{\partial t} = 0 \quad \text{and} \quad \frac{\partial v}{\partial t} = 0 \tag{5}$$
4. **Fully developed flow**: there is no variation in velocity along the x-direction. Thus:
$$\frac{\partial u}{\partial x} = 0 \quad \text{and} \quad \frac{\partial v}{\partial x} = 0 \tag{6}$$
5. **Laminar flow**: the flow being laminar of constant depth, the velocity is null in the direction normal to the plane.
$$v = 0 \tag{7}$$

Boundary conditions

Bottom No-slip wall:

$$u(0) = 0 \tag{8}$$

Top **Open channel flow**: the free surface is a symmetry plane, so the velocity gradient is null and the pressure is equal to the atmospheric pressure:

$$p(h) = p_0 \quad \text{and} \quad \frac{\partial u}{\partial y}(h) = 0 \tag{9}$$

Closed channel flow: simple symmetry condition

$$\frac{\partial u}{\partial y}(h) = 0 \tag{10}$$

Velocity profile u
We thus obtain the simplified differential equations

$$\frac{\partial p}{\partial x} - \rho F_x = \mu \frac{\partial^2 u}{\partial y^2} \tag{11}$$
$$\frac{\partial p}{\partial y} - \rho F_y = 0 \tag{12}$$

Integrating the second equation in y gives:

$$p = \rho F_y\, y + C(x) \tag{13}$$

For the open channel case, we apply the boundary condition $p(h) = p_0$ and recall that h is constant:

$$\begin{aligned} p_0 &= \rho F_y\, h + C(x) \Rightarrow C(x) = -\rho F_y\, h + p_0 \\ p &= -\rho F_y(h - y) + p_0 \\ &= \rho g \cos\theta(h - y) + p_0 \end{aligned} \tag{14}$$

from which we get that

$$\frac{\partial p}{\partial x} = 0 \tag{15}$$

We can also observe that the pressure is linear in depth but not equal to the weight of the column of water directly above the bottom as if the water was still. In fact, the pressure at the bed ($y = 0$) decreases with the slope θ to reach 0 when $\theta = 90°$.

For the closed channel case with channel width $H = 2h$, we first plug eq. (13) in the first momentum equation (1):

$$p = \rho F_y\, y + C(x) \implies \frac{\partial p}{\partial x} = C'(x) \implies C'(x) = \rho F_x + \mu \frac{\partial^2 u}{\partial y^2} \tag{16}$$

Since u is a function of y only and $C'(x) - \rho F_x$ is a function of x only, the above equality is valid only if both sides are constant:

$$\begin{aligned} \mu \frac{\partial^2 u}{\partial y^2} &= C'(x) - \rho F_x = D = \text{constant} \\ \implies \mu \frac{\partial \tau}{\partial y} &= D = \text{constant} \end{aligned} \tag{17}$$

Thus the shear stress is linear in y. Since $F_x = g \sin\theta + f_x$ is user-defined and constant, we can write:

$$\begin{aligned} C'(x) &= D + \rho F_x = \text{constant} \\ \implies C(x) &= (D + \rho F_x)x + C_0 = \frac{\partial p}{\partial x} x + C_0 \end{aligned} \tag{18}$$

Thus the pressure gradient is linear. The pressure gradient is directly defined by the user-defined experiment parameters. In the analytical computations, we can simply consider it as known, while on the 2D numerical model it will be imposed either as a component of the body force or equivalently by setting the pressure boundary conditions $p_1(y)$ and $p_2(y)$ at the inlet and outlet sides. Setting those as constants would be equivalent to neglecting the hydrostatic pressure. To account for the hydrostatic pressure, we need to get the expression of the hydrostatic linear pressure gradient and offset it by a constant: $p_1 = p_{hs}(y) + p_x L$ and $p_2 = p_{hs}(y)$.

$$\begin{aligned} \implies p &= \rho F_y\, y + \frac{\partial p}{\partial x} x + C_0 \\ &= -\rho g \cos\theta\, y + p_x x + C_0 \end{aligned} \tag{19}$$

We obtain the linear hydrostatic distribution added to the linear gradient. C_0 is a constant of integration that will set the absolute pressure offset and can be set to 0.

Substituting into the simplified x-momentum equation:

$$p_x = \rho F_x + \mu \frac{\partial^2 u}{\partial y^2}. \tag{20}$$

$$\iff \frac{\partial^2 u}{\partial y^2} = \frac{p_x - \rho F_x}{\mu} = \frac{p_x - \rho(g \sin\theta + f_x)}{\mu} \tag{21}$$

Integrating twice with respect to y:

$$u = \frac{p_x - \rho F_x}{2\mu} y^2 + Ay + B \tag{22}$$

Applying the boundary condition $u(0) = 0$ and $\frac{\partial u}{\partial y}(h) = 0$:

$$u(0) = 0 \implies B = 0 \tag{23}$$

$$\frac{\partial u}{\partial y}(h) = 0 \implies \frac{p_x - \rho F_x}{\mu} h + A = 0 \implies A = -\frac{p_x - \rho F_x}{\mu} h \tag{24}$$

Thus, the velocity profile is given by:

$$u = \frac{\rho F_x - p_x}{\mu} (hy - \frac{y^2}{2}) \tag{25}$$

We can define $\mathbf{F} = \rho F_x - p_x [Pa\ m^{-1}]$ as the equivalent driving force, which is constant in the flow direction. The velocity profile can then be written as:

$$u = \frac{\mathbf{F}}{\mu} (hy - \frac{y^2}{2}) \tag{26}$$

defining the friction velocity $u_\tau = \sqrt{\frac{\tau_w}{\rho}}$ and $\eta = \frac{y}{h}$, it can be written in dimensionless form:

$$\frac{u}{u_\tau} = u_\tau \frac{h}{\nu} \left(\eta - \frac{\eta^2}{2} \right) \tag{27}$$

Maximum velocity $u_{\mathbf{max}}$

The maximum velocity occurs at $y = h$:

$$u_{\max} = \frac{\rho F_x - p_x}{\mu} \frac{h^2}{2} = \frac{\mathbf{F}}{\mu} \frac{h^2}{2} = u_\tau^2 \frac{h}{2\nu} \tag{28}$$

Flow rate q

The flow rate per unit width is given by:

$$\begin{aligned} q &= \int_0^h u\, dy = \int_0^h \frac{\mathbf{F}}{\mu} (hy - \frac{y^2}{2})\, dy \\ &= \frac{\mathbf{F}}{\mu} \left(\frac{h^2}{2} y - \frac{y^3}{6} \right) \Big|_0^h = \frac{\mathbf{F} h^3}{3\mu} = u_\tau^2 \frac{h^2}{3\nu} \end{aligned} \tag{29}$$

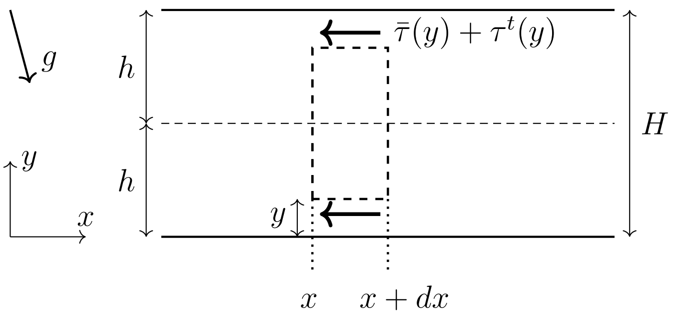

Figure 1: Control volume for the turbulent flow

Bulk velocity U
The bulk velocity is given by:

$$U = \frac{q}{h} = \frac{\mathbf{F}h^2}{3\mu} = u_\tau^2 \frac{h}{3\nu} \tag{30}$$

Reynolds number Re
The Reynolds number for the flow, based on the characteristic length h and velocity U, is given by:

$$Re = \frac{\rho U h}{\mu} = \frac{\rho \mathbf{F} h^3}{3\mu^2} = u_\tau^2 \frac{h^2}{3\nu^2} \tag{31}$$

Shear stress $\tau(y)$
The shear stress depends on y and is given by:

$$\tau(y) = \mu \frac{\partial u}{\partial y} = \mu \left(\frac{\rho F_x - p_x}{\mu}(h - y) \right) = (\rho F_x - p_x)(h - y) = \mathbf{F}(h - y) \tag{32}$$

$$\tau_w = (\rho F_x - p_x)h = \mathbf{F}h \tag{33}$$

Shields number τ^*
The Shields number is given by:

$$\tau^* = \frac{\tau_w}{gd(\rho_s - \rho)} = \frac{(\rho F_x - p_x)h}{gd(\rho_s - \rho)} = \frac{\mathbf{F}h}{gd(\rho_s - \rho)} = \frac{(\rho(g \sin\theta + f_x) - p_x)h}{gd(\rho_s - \rho)} \tag{34}$$

1.2.2 Turbulent fluid flow over an inclined plane

To practically sweep through the higher transport regimes, we said we would have to use additional driving forces on the fluid. We will also have to enter the turbulent regime, thus we need the turbulent version of the equations above. We thus consider a steady, two-dimensional, fully developed flow of water over an inclined plane, with constant flow depth along the streamwise direction. Following the Fluid Mechanics course notes [LW18] and Yalin [Yal77], we define a differential control volume centered in a closed channel as in fig. 1. Since the flow is fully developed, the momentum fluxes at the inlet and outlet are equal, and the forces acting on the fluid are balanced. For these assumptions to make sense, we need to consider the Reynolds-averaged quantities but we will keep the same notation. The forces acting on the fluid are:

- the hydrostatic pressure forces at the left and right boundaries P_l and P_r

- the hydrostatic pressure forces at the top and bottom boundaries P_b and P_t
- the driving pressure forces at the left and right boundaries $P_{l,x}$ and $P_{r,x}$
- the total shear stress $\tau(y)$ acting along the bottom and top boundaries τ_b and τ_t
- the body accelerations in the x and y directions F_x and $F_y = -g\cos\theta$

Since the depth h is constant, the hydrostatic terms cancel each other on the sides $P_r = P_l$ and the pressure gradient in the x direction is constant. By definition of the hydrostatic pressure, the pressure forces and the top and bottom compensate the weight component normal to those boundaries $P_b - P_t = F_y$, such that the fluid does not accelerate in the y direction. The forces exerted by the pressure gradient are given by:

$$P_{l,x} = p(x)hW \tag{35}$$
$$P_{r,x} = p(x+dx)hW \tag{36}$$

With W the width of the channel in the third dimension, which is constant. By symmetry, the shear stress at the top and bottom boundaries are equal $\tau_b = \tau_t = \tau(y)$. The force balance in the x direction is thus given by:

$$\begin{aligned}
P_{l,x} - P_{r,x} + \rho\, V\, F_x &= \tau_b + \tau_t \\
W(2(h-y)\,p(x) - 2(h-y)\,p(x+dx) - 2\,\tau(y)\,dx + \rho\,2(h-y)\,dx\,F_x) &= 0 \\
(h-y)\frac{p(x)-p(x+dx)}{dx} - \tau(y) + (h-y)\,\rho F_x &= 0 \\
(h-y)(\rho F_x - \frac{\partial p}{\partial x}) &= \tau(y) \\
(h-y)(\rho(f_x + g\sin\theta) - \frac{\partial p}{\partial x}) &= \tau(y)
\end{aligned} \tag{37}$$

We thus obtained that the (Reynolds averaged) total shear stress profile is linear in turbulent flow too. Plugging $y = 0$ gives the wall shear stress:

$$\tau_w = \tau(0) = h(\rho F_x - \frac{\partial p}{\partial x}) \tag{38}$$
$$\implies \tau(y) = \tau_w(1 - \frac{y}{h}) \tag{39}$$

This last equation implies that the Shields number expression is the same as in the laminar case, which means the number does not directly account for the turbulent fluctuations' role in the sediment transport process.

Velocity profile u
Following the typical approach in turbulent flow, we will derive the velocity profile. The

usual turbulence variables are defined:

$\nu_t = \dfrac{-\overline{u'\,v'}}{\frac{du}{dy}}$	the effective turbulent viscosity
$u_\tau = \sqrt{\dfrac{\tau_w}{\rho}}$	the friction or shear velocity
$Re_\tau = \dfrac{u_\tau h}{\nu}$	the friction Reynolds number
$Re_{k_s} = \dfrac{u_\tau k_s}{\nu}$	the (sand) roughness Reynolds number
$\eta = \dfrac{y}{h}$	the outer space variable
$u^+ = \dfrac{u}{u_\tau}$	the inner velocity variable
$y^+ = \dfrac{y u_\tau}{\nu}$	the inner space variable

The Reynolds-averaged Navier-Stokes momentum equations for a 2D steady incompressible and fully developed flow are given by:

$$0 = -\frac{dp}{dx} + \rho F_x + \frac{d}{dy}\left[\,\tau_{xy} - \rho\overline{u'v'}\,\right] \tag{40}$$

$$0 = -\frac{dp}{dy} + \rho F_y \tag{41}$$

First we define the tensor of the effective additional stresses due to turbulence or Reynolds stress tensor [LW18] $\tau^t_{ij} = -\rho\overline{u'_i u'_j}$. This quantity is unknown and will need to be modeled using a *turbulence closure model*. For the purpose of our analytical computations, we will limit ourselves to classical algebraic or *zero-equation* models. In analogy with Newton's law of viscosity $\tau_{xy} = \mu\frac{du}{dy}$, Boussinesq was the first to define a "mixing coefficient" which corresponds to an apparent turbulent viscosity or eddy viscosity ν_t [Sch68]:

$$\tau^t = -\rho\overline{u'v'} = \rho\nu_t\frac{du}{dy} \implies \nu_t = -\frac{\overline{u'v'}}{\frac{du}{dy}} \tag{42}$$

Equation (40) can thus be rewritten as:

$$0 = -\frac{dp}{dx} + \rho F_x + \frac{d}{dy}\left[(\mu + \mu_t)\,\frac{du}{dy}\right] = -\frac{dp}{dx} + \rho F_x + \mu\frac{d^2u}{dy^2} + \frac{d}{dy}\left(\nu_t\frac{du}{dy}\right) \tag{43}$$

We now have to model the eddy viscosity ν_t. Starting from Reynolds' decomposition in mean and fluctuating components $u = \bar{u} + u'$, Prandtl[Pra26] was the first to propose a model for the eddy viscosity, based on the very successful kinetic theory of gases. He pictured turbulent fluctuations as coherent "lumps" that hop a characteristic *mixing length* ℓ, analogous to the molecular mean-free-path, across flow layers while carrying the momentum of their origin. Suppose we observe the layer $\bar{u}(y)$ where lumps come from the layers $\bar{u}(y+\ell)$ and $\bar{u}(y-\ell)$, then the spread of velocities at $\bar{u}(y)$ is approximated at the first order by $\pm\ell\frac{d\bar{u}}{dy}$ which means $|u'(y)| \propto \ell\frac{d\bar{u}}{dy}$ [Dav15]. Now still following Prandtl and assuming that the vertical velocity fluctuations v' are produced by collisions of those lumps from other layers, we can expect their order of magnitude to be similar: $u' \simeq v'$. With some sign considerations, he finally got:

$$\tau_t = -\rho\overline{u'v'} \overset{\text{mod}}{=} \rho\ell^2 \left|\frac{d\bar{u}}{dy}\right| \frac{d\bar{u}}{dy} \tag{44}$$

$$\implies \nu_t \overset{\text{mod}}{=} \ell^2 \left|\frac{d\bar{u}}{dy}\right| \tag{45}$$

We still have to model ℓ. As Schlichting notes however, the empirical observation that turbulent drag is roughly proportional to the square of velocity in addition with eq. (44) led to the result that the mixing length is a purely local function $\ell(y)$. Von Kármán [Kár30] later proposed a derivation of eq. (44) based on similarity arguments and confirmed that result [Sch68], while also providing a model for the mixing length:

$$\ell \overset{\text{mod}}{=} \kappa \left|\frac{du/dy}{d^2u/dy^2}\right| \tag{46}$$

Here κ is the von Kármán constant, which is a universal constant of order 0.4. To obtain the velocity profile, we first assume that the flow is fully turbulent so that the laminar (Newton) shear stress can be neglected. Using Kármán's expression as is leads to a logarithmic velocity profile but more complex than the usual form[Sch68]. Instead, Prandtl [Pra33] proposed a simpler model based on the argument that near a wall, but not near enough that the viscous stresses are dominant, a characteristic length scale can be defined as the distance to the wall $\ell \propto y$. This can be interpreted to a point as the fact that the eddies near the wall can only have a smaller radius and travel a distance inferior to the distance to the wall. This leads to the following model:

$$\ell \overset{\text{mod}}{=} \kappa y \tag{47}$$

To obtain a proper logarithmic velocity profile, Prandtl made a further assumption that in the region of validity of the model i.e. near the wall, the (total) shear stress can be considered constant, then proved that the associated profile is equivalent to von Kármán's under this assumption. It is verified by definition for Couette flows but also experimentally in a region near the wall for boundary layers. For inner flows however, the validity of the assumption can seem more questionable with regard to eq. (39) and leads to discussion. Applying it nonetheless, we get the famous logarithmic velocity profile:

$$
\begin{aligned}
\nu_t =& l^2 \frac{du}{dy} = \kappa^2 y^2 \frac{du}{dy} \\
\tau_t =& \rho \nu_t \frac{du}{dy} = \rho \kappa^2 y^2 \left(\frac{du}{dy}\right)^2
\end{aligned}
$$

$$
\Bigg\downarrow
\begin{array}{l}
\text{Fully developed turbulent region: } \tau \simeq \tau_t \iff \tau_l \simeq 0 \qquad (48) \\
\tau(y) = \tau_w (1 - \frac{y}{h}) \qquad (39)
\end{array}
$$

$$\tau_w (1 - \frac{y}{h}) = \rho \nu_t \frac{du}{dy} \tag{49}$$

$$\Big\downarrow \text{Prandtl mixing length: } \nu_t = \ell^2 \frac{du}{dy} \tag{50}$$

$$\tau_w (1 - \frac{y}{h}) = \rho \ell^2 \left(\frac{du}{dy}\right)^2 \tag{51}$$

$$\big\downarrow \text{Prandtl m.l. profile: } \ell = \kappa \, y \tag{47}$$

$$\tau_w (1 - \frac{y}{h}) = \rho \kappa^2 y^2 \left(\frac{du}{dy}\right)^2$$

$$\Big\downarrow \text{Prandtl assumption: } \tau(y) = (1 - \frac{y}{h}) \tau_w \simeq \tau_w \iff \frac{y}{h} << 1 \tag{52}$$

$$\tau_w = \rho \kappa^2 y^2 \left(\frac{du}{dy}\right)^2$$

$$\frac{u_\tau}{\kappa y} = \frac{du}{dy} \tag{53}$$

$$\frac{u}{u_\tau} = \frac{1}{\kappa} \ln y + A \tag{54}$$

And we get the generic logarithmic law. From there we can derive the several common forms. Equation (56) and eq. (57) are the most common forms in hydraulics works.

$$a)\ A = \ln \frac{u_\tau}{\nu} + C \qquad \implies u^+ = \ln y^+ + C \tag{55}$$

$$b)\ u(y_0) = 0 \implies A = -\frac{1}{\kappa} \ln y_0 \qquad \implies \frac{u}{u_\tau} = \frac{1}{\kappa} \ln \frac{y}{y_0} \tag{56}$$

$$c)\ u(y_0) = u_0 \implies A = \frac{u_0}{u_\tau} - \frac{1}{\kappa} \ln y_0 \qquad \implies \frac{u}{u_\tau} = \frac{1}{\kappa} \ln \frac{y}{y_0} + \frac{u_0}{u_\tau}$$

$$c_{bis})\ \begin{cases} B = \frac{u_0}{u_\tau} \\ k_s = y_0 \end{cases} \implies B = C + \frac{1}{\kappa} \ln k_s^+ \implies \frac{u}{u_\tau} = \frac{1}{\kappa} \ln \frac{y}{k_s} + B \tag{57}$$

We defined the roughness length k_s which is the representative length of the asperities of the wall surface. A more modern derivation of this law is given by Pope [Pop00], based on dimensional analysis instead of the mixing length concept. Equation (48) is equivalent to the definition of the outer region $\nu << \nu_t$, while eq. (52) is the definition of the inner region [Pir14]. The region where both conditions are met is the overlap region[Pop00]. Experimental observations showed that eq. (55) is verified in the overlap region and even further in the outer region [Yal77], especially for open channel flows. G. Winckelmans [LW18] mentions that the observed eddy viscosity profile can be fit more accurately with a parabola on recent DNS data in a way assumption (52) is not needed to derive the log law. In fact, if we work the reasoning backwards from the log law result eq. (55), and we take the ODE for the outer region eq. (51) we find:

$$
\begin{aligned}
\tau_w(1-\frac{y}{h}) =& \rho\ell^2\left(\frac{du}{dy}\right)^2 && (51)\\
&\Big\downarrow \frac{u}{u_\tau} = \frac{1}{\kappa}\ln\frac{y}{y_0} \iff \frac{du}{dy} = \frac{u_\tau}{\kappa y} && (53)\\
\tau_w(1-\frac{y}{h}) =& \rho\ell^2\frac{u_\tau^2}{\kappa^2 y^2} && (58)\\
\ell =& \kappa y\sqrt{1-\frac{y}{h}} && (59)\\
&\Big\downarrow \frac{du}{dy} = \frac{u_\tau}{\kappa y} && (53)\\
\nu_t =& u_\tau \kappa y\left(1-\frac{y}{h}\right) && (60)
\end{aligned}
$$

Plugging the obtained turbulent viscosity ν_t in the ODE eq. (49) the terms $\left(1-\frac{y}{h}\right)$ do cancel to lead to the log law without the need for assumption 52. Kundu et al. [KKG18] attribute eq. (59) to Prandtl. The log law is valid under the assumption that the dominant shear stress component is turbulent eq. (48), which is not verified in the direct vicinity of the wall. In fact, it is the laminar shear stress τ_l that is dominant in this region called the laminar sublayer, which only exists with *smooth enough* walls.

$$
\begin{aligned}
\tau_l =& \rho\nu\frac{du}{dy} && (61)\\
&\Big\downarrow \text{Laminar sublayer: } \tau \simeq \tau_l && (62)\\
\tau_w(1-\frac{y}{h}) =& \rho\nu\frac{du}{dy} && (63)\\
&\Big\downarrow \text{Inner region: } \frac{y}{h} << 1 && (64)\\
u_\tau^2 =& \nu\frac{du}{dy}\\
u =& u_\tau^2\frac{y}{\nu}\\
u^+ =& y^+ && (65)
\end{aligned}
$$

As mentioned the inner region assumption is equivalent to eq. (52). We thus obtain that the velocity profile is linear in the laminar sublayer. Yalin [Yal77] discusses the validity of the log law in the overlap and outer regions with regard to assumption 52 in more depth and concludes at the time that it is reasonable to use it up to the surface of open channel flows, while the laminar sublayer is negligible for depth averaged quantities. Nezu and Rodi [NR86] later reinvestigated the question with new measurement methods and concluded that the wake effect was more pronounced than previously thought in open channel flows. They applied Van Driest [Van56] damping function to model the transition region between the laminar sublayer and the overlap region, and Coles' [Col56] wake function for the outer region. They also investigated the mixing length but with difficulties to measure reliably the region near the surface. The mixing length incorporating Van Driest damping function and

Coles' wake function they used is:

$$\frac{\ell}{h} = \kappa\sqrt{1-\eta}\left[\frac{1}{\eta} + \pi\Pi\sin(\pi\eta)\right]^{-1}\left(1 - \exp\left(-\frac{\eta Re_\tau}{A^+}\right)\right) \tag{66}$$

This model gives the correct asymptotes in the laminar sublayer and the overlap region in a single equation thanks to Van Driest damping function, and captures the wake thanks to Coles' function. It needs to be numerically integrated, however. One can see that when Coles' parameter Π is set to 0 and Van Driest damping function $\Gamma(\eta, Re_\tau, A^+) = \left(1 - \exp\left(-\frac{\eta Re_\tau}{A^+}\right)\right)$ ignored, the mixing length profile reduces to the form associated with the quadratic turbulent viscosity profile eq. (59) and the classic log law is recovered. The parameter A^+ is a constant that depends on the flow conditions and is typically set to 26. Nezu and Rodi applied this profile with very good success for their smooth open channel flume measurements. A comparison of the mixing length models eq. (47), eq. (59) and eq. (66) is shown in fig. 2a. Alongside are shown the open channel DNS data of Yao, Chen, and Hussain [YCH22] for the smooth case, Chan-Braun, García-Villalba, and Uhlmann [CGU11] for the rough case with a resolved bed of spheres, and also the experimental data from Rousseau and Ancey [RA22] and Voermans, Ghisalberti, and Ivey [VGI17]. Openly available recent DNS and experimental data on open channel flows is scarce and even more so with resolved immobile grain beds. On fig. 2b are shown the associated velocity profiles. Voermans data has been discarded for the velocity profiles because it does not show a clear log law region, while Rousseau's data does show a log law region. All selected runs have a similar friction Reynolds number $Re_\tau \approx 180$. Since the bed is not clearly defined in the case of grain or sphere beds, authors use different methods to fix the origin of the vertical coordinate.

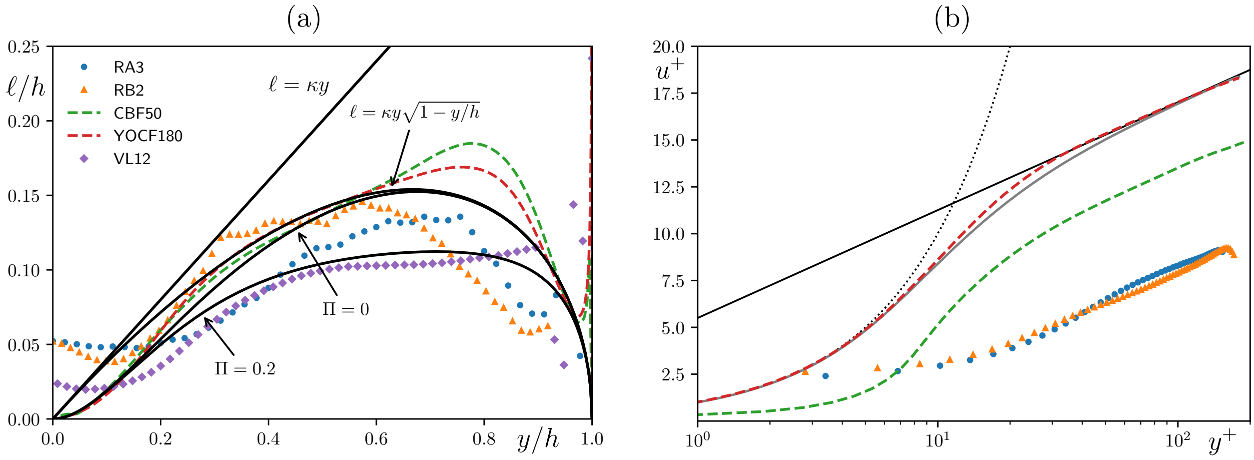

Figure 2: (a) Mixing length profiles for different models (black lines). Black curves in (a) indicating a Coles' wake parameter Π are plotted from eq. (66) with $A^+ = 27$, as well as the gray curve in (b) which is plotted using the parameters of YOCF180 DNS case. DNS data from [YCH22] and [CGU11] (dashed lines) and experimental data by [RA22] and [VGI17] (markers). The run labels are composed of the authors initials and associated runs in their respective papers. Example: CBF50 corresponds to [CGU11] run labelled F50.

Derived quantities

In this work, since we will use the velocity profile and derived equations to estimate what the experiment external parameters should be depending on the flow conditions we want to reproduce, we will limit ourselves to eq. (55) with the roughness function $B(Re_{ks})$ from

[Yal77] to account for the different roughness regimes depending on the grain size. Since we use a purely logarithmic model without wake function, we also will not discriminate between open and (half) closed channel flows. This is for the sake of simplifying the systems of equations in the turbulent case. The derived quantities are given below. Note that the problem of the origin of the log law, discussed by Karra et al. [Kar+23] in the case of a bed of spheres, is not addressed for the same reason and the origin is set to 0 for computations, which corresponds to h_p in the simulation domain presented in the next sections.
First let us remind the friction velocity is given by:

$$u_\tau = \sqrt{\frac{\tau_w}{\rho}} = \sqrt{\frac{\mathbf{F}h}{\rho}} \tag{67}$$

Friction Reynolds number Re_τ
The friction Reynolds number is defined as:

$$Re_\tau = \frac{u_\tau h}{\nu} = \frac{\sqrt{\tau_w/\rho}h}{\nu} = \frac{\sqrt{\mathbf{F}h/\rho}h}{\nu} = \frac{\sqrt{\mathbf{F}}h^{3/2}}{\sqrt{\rho}\nu} \tag{68}$$

Roughness Reynolds number Re_{ks}
The roughness Reynolds number is defined as:

$$Re_{ks} = \frac{u_\tau k_s}{\nu} = \frac{\sqrt{\tau_w/\rho}k_s}{\nu} = \frac{\sqrt{\mathbf{F}h}k_s}{\nu\sqrt{\rho}} \tag{69}$$

And is equivalent to the particle or granular Reynolds number Re_p for Nikuradse's sand roughness $k_s = d$ or $k_s = d_{50}$.
Maximum velocity $u_{\mathbf{max}}$
The maximum velocity occurs at $y = h$:

$$u^+_{max} = \frac{u_{\max}}{u_\tau} = \frac{1}{\kappa}\ln\frac{h}{k_s} + B(Re_{k_s}) \tag{70}$$

Bulk velocity U
The bulk velocity is defined as the flow rate per unit width divided by the flow depth, and assuming $k_s/h << 1$:

$$U \approx \frac{1}{h}\int_0^h u(y)\,dy = u_\tau\left(\frac{1}{\kappa}\left[\ln\left(\frac{h}{k_s}\right) - 1\right] + B(Re_{k_s})\right) \tag{71}$$

$$U^+ = \frac{U}{u_\tau} = \frac{u_{max}}{u_\tau} - \frac{1}{\kappa} \tag{72}$$

Flow rate q
The flow rate per unit width is given by:

$$q \ = Uh = u_\tau h\left(\frac{1}{\kappa}\left[\ln\left(\frac{h}{k_s}\right) - 1\right] + B(Re_{k_s})\right) \tag{73}$$

Reynolds number Re
The Reynolds number for the flow, based on the characteristic length h and velocity U, is given by:

$$Re = \frac{\rho U h}{\mu} = \frac{\rho h u_\tau}{\mu}\left(\frac{1}{\kappa}\left[\ln\left(\frac{h}{k_s}\right) - 1\right] + B(Re_{k_s})\right) \tag{74}$$

$$= Re_\tau U^+ \tag{75}$$

1.3 Sediment transport

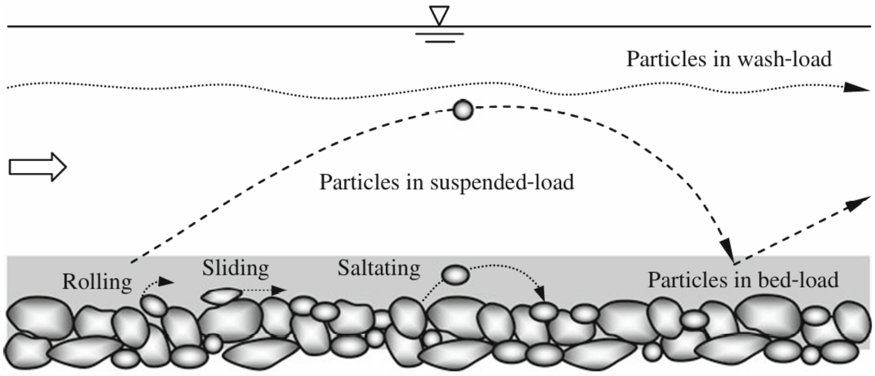

Figure 3: Transport modes for sediment particles in a fluid. Figure 5.1 in Dey [Dey24].

1.3.1 Incipient motion

One classical problem of sediment transport is to predict the strength of the flow it is submitted to at which some particles start to move. This condition is often translated into a *critical shear stress* and depends on fluid, flow and particle properties. The forces acting on a particle at rest on the top of a bed of grains over which a fluid flows are:

i the weight of the particle $W = \rho_s g V$

ii the buoyancy force $B = \rho g V$

iii the drag force F_d

iv the lift force F_l

v the normal contact forces with the contacting grains F_n

vi the friction force with the contacting grains F_f

in which (i) is a body force, (ii), (iii) and (iv) are fluid forces and (v) and (vi) are contact forces. The net weight of the particle is given by $W - B = (\rho_s - \rho)gV$. The fluid force depends heavily on the particle Reynolds number $Re_p = \frac{\rho u d}{\mu}$.

Following Southard [Sou06a], we can apply a force balance on a single grain. Assume the friction does not permit the grain to slide on the others and the dominant fluid force is drag. To simplify, we consider the 2D case. To detach from the bed, the torque exerted by the fluid forces must overcome the torque exerted by the net weight of the grain F_G. Denote α the angle of the contact plane with the bed plane and $\mathbf{r}_G$ the radius vector starting from the center of mass of the grain to the contact point. Denote $\mathbf{l}_D$ the lever arm vector from the equivalent center of application D of the drag force, which depends on the shear stress distribution on the grain surface and is not known a priori, to the contact point. See fig. 4 Then the torque balance is written as:

$$\mathbf{F}_D \times \mathbf{l}_D = \mathbf{F}_G \times \mathbf{r}_G \tag{76}$$

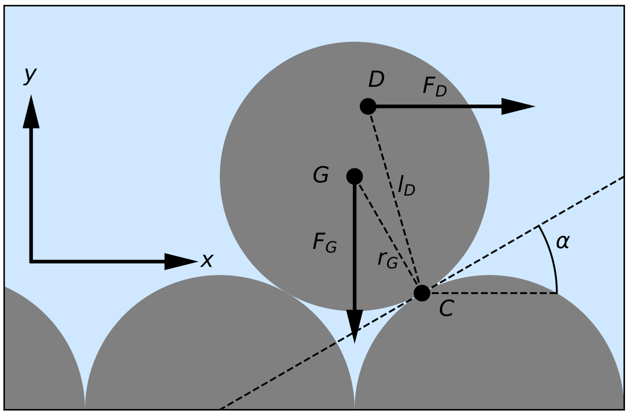

Figure 4: Diagram of the force balance on a single grain at the threshold of motion.

then defining a_D as a coefficient taking account of the unknown drag application point and lever arm length, we can write:

$$a_D F_D \cos\alpha = (\rho_s - \rho)\ V\ r_G g \sin\alpha \tag{77}$$

Then noting c_1 a shape coefficient that depends on the particle shape, the volume is expressed as $V = c_1 d^3$. The fluid drag force can be estimated using Stokes' law with a slip velocity $U \sim cd\frac{du}{dy}$ with an exposition factor c, which gives $F_D \sim c_2 d^2 \tau_w$ where the coefficient c_2 depends on the drag coefficient, the particle shape and the packing geometry.

$$a_D c_2 d^2 \tau_w \cos\alpha = (\rho_s - \rho)\ c_1 d^3\ r_G g \sin\alpha \tag{78}$$

Rearranging and noting τ_c for the critical shear stress at which motion starts, we get:

$$\tau_c = (\rho_s - \rho) g d \frac{r_G c_1}{a_D c_2} \tan\alpha \tag{79}$$

Or in dimensionless form and defining the submerged specific weight $\gamma' = (\rho_s - \rho)g$:

$$\tau_c^* = \frac{\tau_c}{\gamma' d} = \frac{r_G c_1}{a_D c_2} \tan\alpha \tag{80}$$

The failure mode or erosion mode we have just investigated (a simplified version) to introduce the Shields number is drag-induced rolling. One can also apply the same reasoning sliding, which would introduce the grain friction coefficient in the right-hand side, but also for lifting and the effects of turbulence and cohesion. A complete analytical inventory of erosion modes and their respective critical Shields number curves, as well as their effect on the total curve, is given by Miedema [Mie10; Mie12]. The left-hand side of eq. (80) was obtained by Shields [Shi36] by using dimensional analysis arguments and is called the Shields number, or Shields parameter. From his analysis, it is established that the variables controlling incipient motion of cohesionless grains in a Newtonian fluid are $\{\rho, \mu, \gamma', d, \tau_w\}$, where $\gamma' = (\rho_s - \rho)g$ is the submerged specific weight. With three base dimensions (M,L,T), Buckingham–Π implies two independent dimensionless variables. A common choice, using the set of *repeating variables* (τ_w, ρ, d) is

$$\Pi_1 = \frac{\tau_w}{\gamma' d} \equiv \tau^* \quad \text{(Shields number)}, \qquad \Pi_2 = \frac{\rho u_* d}{\mu} \equiv Re_p, \quad \text{(particle Reynolds number)}, \tag{81}$$

Hence the threshold relation can be written as

$$\tau_c^* = f(Re_p) \tag{82}$$

Where τ_c^* is called the critical Shields number and is a threshold for the start of motion (erosion). Other common choices for Π_2 are the Galileo number $Ga = \sqrt{\gamma' d^3/(\rho\nu^2)}$ or the "dimensionless grain size" $D_* = d\big(\gamma'/(\rho\nu^2)\big)^{1/3}$. These are related by

$$Re_p^2 = \tau^* \, Ga^2 = \tau^* \, D_*^3 \tag{83}$$

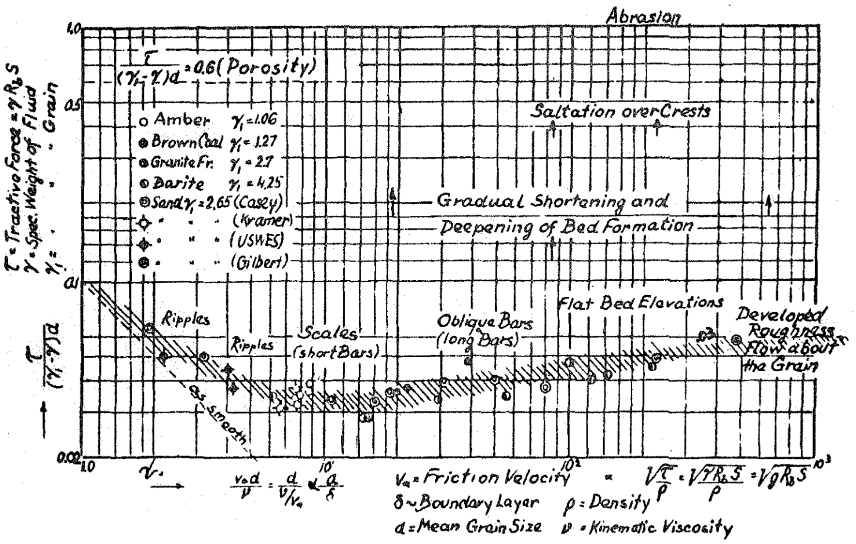

Fig. 6. Tractive - force coefficient $\frac{\tau}{(\gamma_1 - \gamma)d}$ against the Reynolds number of the grain $\frac{V_* d}{\nu}$.

Figure 5: Original (translated) Shields diagram, showing the critical Shields number τ_c^* (hashed area) for threshold of motion as a function of the particle Reynolds number Re_p.

Shields obtained from experiments the diagram presented on fig. 5, indicating the value of the critical Shields number depending on Re_p. The threshold stays roughly in the same order of magnitude over $1 < Re_p < 10^3$. The variations, which are not trivial to explain and are developed by Miedema [Mie12], will not be explained in this work as we do not focus on the threshold of motion. The use of Shields number is not limited to incipient motion as will be seen later.

1.3.2 Bed load

In this work we are most interested in intense bed load configurations. Southard [Sou06b] defines bed load as particle load which travels in direct contact with the bed or so close to the bed as not to be substantially affected by the fluid turbulence. The sediment load in fluids is also found in the form of suspended and wash load, the difference being that the particles types found in the wash load are not found in the bed we look at, meaning they were transported over long distances in suspension. Bed load occurs mostly via rolling, sliding and saltation; short ballistic hops with repeated impacts on the bed, see fig. 3.

Pioneering work on strongly sheared sediment beds was done by Bagnold [Bag54] with an annulus shear cell and neutrally buoyant particles. He observed that particles exerted dispersive normal stresses on the annulus walls. Bagnold [Bag56] then extended his work to the case of higher density particles in a channel. He states that if the flow is strong enough, a layer of transported sediments several diameters thick can form just above the bed in which that dispersive stress maintains the bed-load layer in this "flowing" state. This *sheet flow* layer has been observed to behave like a viscous fluid and to maintain a clear boundary with the above flow, sometimes called *traction carpet* or *rheological layer*.

1.3.3 Sediment transport rate

Still following Southard [Sou06b], the sediment load per unit area of bed is defined as the depth-integrated sediment mass concentration profile $c(y)$ at that point:

$$L_s = \int_0^h c(y)\, dy \tag{84}$$

If $c(y)$ is given in $[kg/m^3]$, then L_s is in $[kg/m^2]$.

We define the area concentration ϕ as the ratio between the area occupied by the particles and the area occupied by the fluid, which is equivalent to the solid fraction.

$$\phi(y) = \frac{dA_p}{dA_f}(y) \tag{85}$$

Then the volumetric sediment flow rate per unit width $q_s[m^2/s]$ can be defined as the integral of the product of the area concentration and the velocity profile of the solid phase $u_s(y)$, also called the local particle flux density $j_s(y) = \phi(y)u_s(y)$:

$$q_s = \int_0^h \phi(y)u_s(y)\, dy \tag{86}$$

Applying the dimensional analysis principles we have seen, we can define a set of variables of which we can expect q_s to depend. We can develop how each term can influence the transport rate.

- The fluid forces on the particles, are what moves the particles. These forces involve the fluid properties $\{\rho, \nu\}$ and the flow properties $\{d, h_f, \tau_w\}$. The most obvious effect is by drag laws which directly influence entrainment and the relative velocity profile. The fluid flow depth h_f is added to the set, which could not reasonably influence the threshold for incipient motion earlier since this threshold is defined at the bed surface. It affects turbulent diffusion of particles and the velocity profile.

- The submerged weight of particles, which resists grain entrainment at the bed and brings them back at the bed, is given by the submerged specific weight $\gamma' = (\rho_s - \rho)g$. A low submerged weight means the particles necessitate less entrainment forces to be mobilised and are transported for longer.

- The relative density ρ_s/ρ can have an additional effect to the submerged specific weight, since inertia difference can influence the response time to a fluid force. Its effect on the threshold for incipient motion has be neglected and is debated [Sou06b].

- The particle size distribution can influence grain arrangement which can make a large difference between monodisperse and polydisperse beds, since monodisperse can have dense crystalline arrangements. In this regard, one could argue it could also have been included for the threshold of movement, instead of including all arrangement considerations in the geometrical constants. The size of the grains also affects their respective settling velocities and suspension time, which have direct effects on the transport rate. We assume the distribution is well represented by the median $d = d_{50}$ and the standard deviation σ.

- The bed forms are neglected in this work

The new set is $\{q_s, \rho, \nu, \tau_w, d, h_f, \rho_s, \sigma, \gamma'\}$. Then we can use the same set of repeating variables as before $\{\tau_w, \rho, d\}$ to get the two dimensionless parameters already defined above and define the other commonly used dimensionless variables:

$$\frac{d}{h_f}, \quad s = \frac{\rho_s}{\rho}, \quad \frac{\sigma}{d} \tag{87}$$

Einstein [Ein50] pioneered the statistical and stochastic description of sediment transport and obtained the dimensionless transport rate form we can then use:

$$q_s^* = \frac{q_s}{\sqrt{\frac{\gamma'}{\rho}d^3}} = \frac{q_s}{\sqrt{(s-1)gd^3}} = f\left(\tau^*,\ Re_p,\ s,\ \frac{d}{h_f},\ \frac{\sigma}{d}\right) \tag{88}$$

Aussillous et al. [Aus+13] proposed a dimensionless transport rate more adapted to laminar flows, which is given by:

$$q_{sl}^* = \frac{q_s}{\frac{(s-1)gd^3}{\nu}} \tag{89}$$

We can also, following Ouriemi [Our07], identify the settling velocity term and use Galileo or Archimedes numbers:

$$Ga = \sqrt{\frac{(s-1)gd^3}{\nu^2}}, \quad Ar = \frac{(s-1)gd^3}{\nu^2} \quad \text{with} \quad Ga = \sqrt{Ar} \quad \text{and} \tag{90}$$

so that we can write:

$$q_s^* = \frac{q_s}{\sqrt{(s-1)gd^3}} = \frac{q_s}{Ga\ \nu} = \frac{q_s}{0.57 w_{s,t}\ d} \quad \text{(classical Einstein form)} \tag{91}$$

$$q_{sl}^* = \frac{q_s}{\frac{(s-1)gd^3}{\nu}} = \frac{q_s}{Ar\ \nu} = \frac{q_s}{18 w_{s,St}\ d} \quad \text{(Aussillous \& Ouriemi form)} \tag{92}$$

where $w_{s,t}$ is the Newtonian settling velocity and $w_{s,St}$ is Stoke's settling velocity:

$$w_{s,t} = \sqrt{\frac{4}{3}\frac{(s-1)gd}{C_D}} = 1.74\sqrt{(s-1)gd} \quad \text{with } C_D \simeq 0.44 \text{ for } 10^3 < Re_s < 10^5 \tag{93}$$

$$w_{s,St} = \frac{1}{18}\frac{(s-1)gd^2}{\nu} \quad \text{for } Re_s < 1 \text{ with } Re_s = \frac{w_s d}{\nu} \tag{94}$$

The dimensionless transport rate q_s^* defined here is also often called the bed-load transport intensity and noted Φ or q_b^* [Dey24].

1.3.4 Sheet flow scaling behavior

The vast majority of the sediment transport literature is devoted to turbulent conditions of the main flow. However, in recent years, there has been a growing interest in the study of sediment transport under laminar bulk flow. One of the first attempts was made by Bagnold [Bag54], however. The study of the internal profiles and structure of intense bed load is also quite recent due to the advancements of measurement equipment, measurement techniques and computational power.

We call *sheet flow* a regime of intense bed load in which a dense mobile granular layer of thickness δ of several grains diameter forms, overlaying the bed in strongly sheared flows. Capart and Fraccarollo [CF11] define it explicitly as a "rapidly sheared transport layer, multiple grains thick" formed along a granular bed. In turbulent conditions, Hsu, Jenkins, and Liu [HJL04] describe sheet flow as arising when shear stresses are sufficient to wash out bedforms and advect a highly concentrated near-bed layer; operationally, some authors locate its upper boundary at the height where particle interdistance is roughly equal to a particle diameter. Consistent with this, Revil-Baudard and Chauchat [RC13] characterise turbulent sheet flow by $\tau^* \gtrapprox 0.5$, a flat bed, and a bed-load layer thickness $\delta \sim \mathcal{O}(10d)$, with grain-grain collisions/friction and turbulence controlling momentum and particle diffusion. In laminar shearing flows, the same structural notion appears under the term "mobile granular layer": a dense, multi-grain-thick layer set into motion above a static bed, with grains predominantly rolling/sliding in sustained contact. Thus, we will use the term in both laminar and turbulent conditions to denote a dense, sheet-like mobile layer over a flat bed.

A lot of different empirical formulas, called sediment discharge formulas, have been developed to express the sediment transport rate q_s^* as a function of the other parameters, most commonly the Shields number τ^* and the critical Shields number τ_c^* (which would have been redundant to add to the variables above, since we added all of its dependencies). A table listing the most common formulas and their *range of validity* is given in [Cha04], table 10.1. A similar table along with a more recent list adapted to the laminar case is given by Ouriemi, Aussillous, and Guazzelli [OAG09].

The first to propose such a formula was du Boys in 1879. He assumed the grains slide over each other at the bed in distinct layers and that the velocity distribution of these layers is linear in y and arrived at the following formula:

$$\begin{aligned} q_s &= \chi \tau_w (\tau_w - \tau_c) \\ q_s^* &= \frac{\chi}{\sqrt{(s-1)gd^3}} \tau^* (\tau^* - \tau_c^*) \gamma'^2 d^2 \\ &= \tau^* (\tau^* - \tau_c^*) \left[\chi \sqrt{\gamma'^3 \rho d} \right] \end{aligned} \tag{95}$$

with, from Schoklitsch, $\chi = \frac{0.54}{\gamma'}$ [Dey24]. His assumptions ended up being disproven but the resulting curve provides a good fit. This type of transport formula is thus based on the *excess bed shear stress* $\tau_w - \tau_c$ or the excess Shields number $\tau^* - \tau_c^*$ and they are called *du Boys type equations*. Shields [Shi36] proposed a very similar empirical formula, which in Einstein form comes down to:

$$\begin{aligned} q_s^* &= \frac{10\, U}{s \sqrt{(s-1)gd}} \, \tau^* \left(\tau^* - \tau_c^* \right) \\ &= \frac{17.4\, U}{s\, w_{s,t}} \, \tau^* \left(\tau^* - \tau_c^* \right) \end{aligned} \tag{96}$$

A widely used formula is the one proposed by Meyer-Peter and Müller [MM48]:

$$q_s^* = 8(\eta_C \tau^* - \tau_c^*)^{1.5} \tag{97}$$
$$\text{with } \eta_C = \left(\frac{C_R(\frac{k_s}{h})}{C_R'(d_{90})} \right)^{1.5}$$

if we assume $k_s \simeq d_{90}$ then we can write:

$$q_s^* = 8(\tau^* - \tau_c^*)^{1.5} \tag{98}$$

Capart and Fraccarollo [CF11] validated the dependence on the $\frac{3}{2}$th power of a Shields number slightly modified to take into account the effect of the slope *on the grains*. They also propose a relation for the mobile layer thickness and found that for "moderate" Shields numbers $\tau^* \lessapprox 1$, the scaling comes down to

$$\delta^* = \frac{\delta}{d} \propto \tau^{*1/2} \quad \text{for } \theta^* \lessapprox 1 \tag{99}$$

while it separates on the lower side for higher Shields numbers.

Ouriemi [Our07], using their 2-phase model, proposed a scaling law for laminar sheet flow which comes down to a cubic law;

$$q_s^* \propto \left(\frac{\theta^*}{\theta_c^*} \right)^3 \quad \text{for } \theta_c^* << \theta^* \tag{100}$$

far enough from the onset of motion, where their continuum approach makes sense. They also proposed a linear scaling for the mobile layer thickness:

$$\delta^* \propto \frac{\theta^*}{\theta_c^*} \quad \text{for } \theta_c^* << \theta^* \tag{101}$$

In their experiments, Ouriemi [Our07] did not recirculate grains and ran the experiment between one day and one week to reach the cessation of motion at the imposed pipe flow rate. Note that with a continuously eroding bed, the Shields number evolves with time too. They found a laminar threshold of motion of $\tau_c^* \approx 0.12$, about double the typical threshold in turbulent conditions.

Interface-resolved DNS by Kidanemariam and Uhlmann [KU14] confirms $q_p \propto \theta^3$ once $\tau^* > \tau_c^* \simeq 0.12$, while finding the mobile-layer thickness grows roughly quadratically with τ^*, steeper than the linear trend predicted by Ouriemi's continuum model under their conditions. They showed that the revision of Ouriemi's model by Aussillous et al. [Aus+13] and in the range of Shields number used for this revision, tends to a quadratic scaling of the mobile layer thickness too when increasing the Shields number, which suggests they did not have enough data in the low Shields number range to observe this quadratic scaling. The fact that the revision is only valid for large enough Shields stress is expected since the continuum modeling is not valid for low Shields numbers, where the mobile layer thickness can be smaller than a grain diameter.

1.3.5 Sheet flow profiles

In this work we will be interested with the internal structure and the profiles of different variables in the sheet flow regime. The rest of this section serves to give an idea of what those

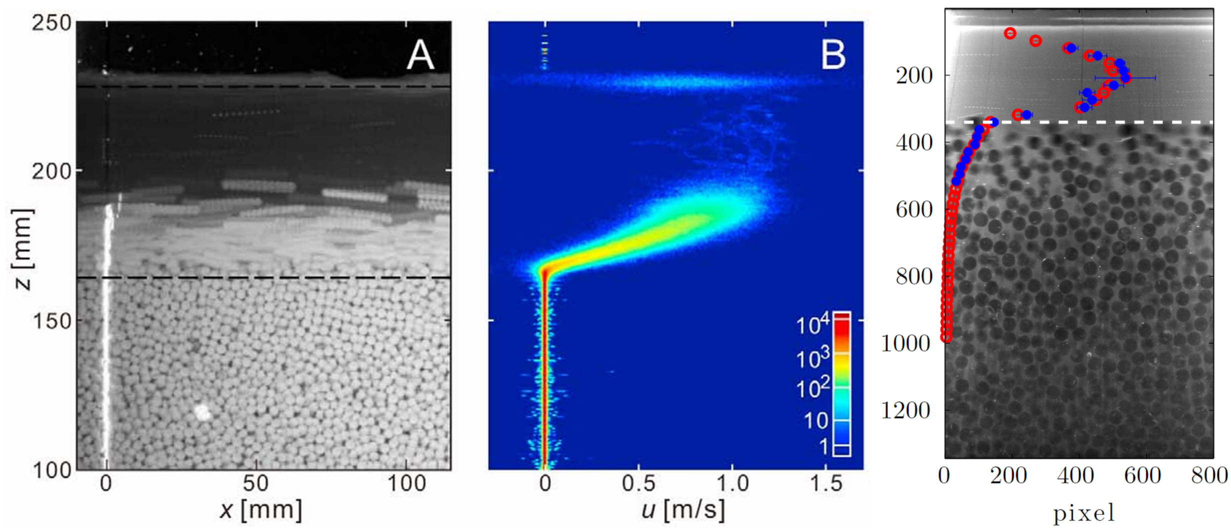

(a) (b)

Figure 6: Examples of sheet flow flume experiment measurements. (a) (A) Snapshot of the flume under sheet flow regime with turbulent bulk flow; (B) and corresponding velocity measurements from Capart and Fraccarollo [CF11] (Fig. 2) using Particle Tracking Velocimetry (PTV) with the frequency of samples (color scale). Horizontal lines denote the bed and free surface levels.(b) Snapshot of the flume under sheet flow regime with laminar bulk flow and the solid (red) and fluid (blue) velocity profile overlays from Aussillous et al. [Aus+13] (Fig. 2) using Particle Image Velocimetry (PIV).

profile should look like. On fig. 6 are shown two examples of flume sheet flow experiments and the corresponding velocity profiles, from [CF11; Aus+13]. Aussillous et al. [Aus+13] used Particle Image Velocimetry (PIV) on both grains and small Stokes number tracer particles to measure velocity profiles and calibrated grayscale imaging to measure the concentration profile with mitigated performance (needs high contrast). Capart and Fraccarollo [CF11] used Particle Tracking Velocimetry (PTV) to measure only the solid velocity profile and laser-stripe estimation of the particle-wall distance to estimate the concentration.

Revil-Baudard et al. [Rev+15] state that the data from Capart and Fraccarollo [CF11] was the only dataset offering both concentration and particle velocity profiles under open channel sheet flow conditions at the time (2015), which gives an idea of the difficulty of sheet flow measurement and the recent advancements. They add that it suffers from the fact that the data is not collocated nor synchronised, and that the measurements are made at the sidewall where the latter affects the flow. A lot of experimental data, like obtained by Capart and Revil-Baudard, does not include the fluid velocity alone, because it is either not measured at all (Capart, PTV) or not measured independently of the solid phase (Revil-Baudard, ACVP). That means the slip between the two phases cannot be analysed.

In turbulent and intense bed load conditions, Capart and Fraccarollo [CF11] found that there exist a striking linear region in the velocity and concentration profiles, as seen on fig. 7a. Revil-Baudard et al. [Rev+15] confirmed this observation to an extent as seen on fig. 7b, running experiments at generally lower Shields numbers than Capart, and found that the linear region is at an inflection point between an exponential region from the bed, and a logarithmic region to the free surface. The latter observation has been confirmed with the presence of a linear region for the mixing length profile in the lower suspension layer. The value of the fitted von Kàrmàn constant however, of $\kappa = 0.225$, reveals the

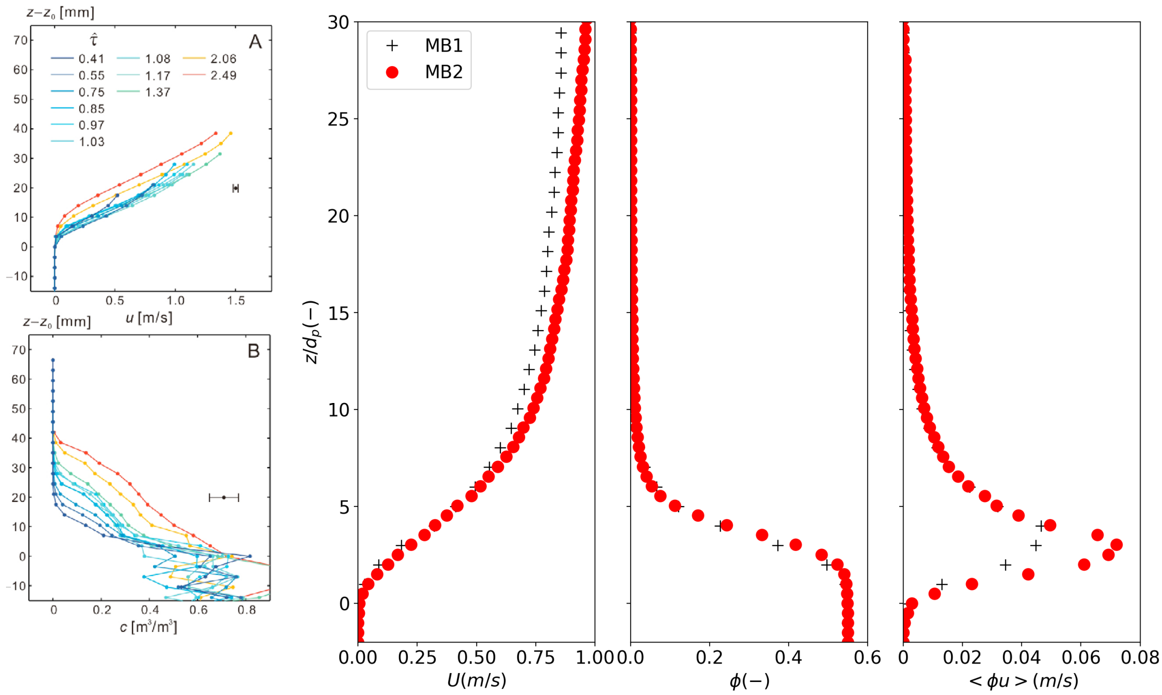

(a) (b)

Figure 7: Examples of sheet flow profiles in turbulent conditions. (a) (A) Solid velocity profiles for different Shields number noted $\hat{\tau}$ and (a) (B) concentration profiles for the same runs from Capart and Fraccarollo [CF11] (Fig. 3). The linear region is clearly identifiable in both cases. (b) Mixed-phase streamwise velocity (left), concentration (middle) and solid flux density (right) profiles from Revil-Baudard et al. [Rev+15] (MB1: $\tau^* = 0.4$) and [Rev+16] (MB2: $\tau^* = 0.5$). At lower Shields number, the linear region is smaller but still present. The solid flux density presents a maximum in the sheet flow layer.

variability of this parameter in sediment-laden flows and the damping effect of the grains on the turbulent mixing in these conditions. Furthermore, they found that effect (the lowering of the von Kàrmàn constant) persists higher in the fluid where the concentration is nearly zero, suggesting that the impact of the sheet flow layer on turbulence is not local. The flux profile from [Rev+15] is also shown on fig. 7b. It shows an asymmetric bell curve with a maximum in the sheet flow layer but does not seem to be centered in the layer and instead lies lower since the concentration gradient is larger than the velocity gradient and that is where the first "knee" of the concentration profile is. A cumulative plot of the concentration would show that roughly half of the transport occurs under the maximum, which implies the other half happens above it and the maximum is situated at half the cumulative transport. Above the linear layer, the concentration profile decreases exponentially to the free surface and the experimental data shows a good agreement with the classic Rouse profile. Revil-Baudard et al. [Rev+15] also confirmed that the mobile layer is further divided in a frictional (of height ϵ in Capart and Fraccarollo [CF11]) layer capped by a collisional layer. It agrees with the shape of the (solid) mixing length profile which tends to diverge towards the bed, which Revil-Baudard et al. [Rev+15] attributes to the lengthening of the contact chains the deeper we look into the bed. In contrast, the fairly constant mixing length $\ell_s \approx 0.5d$ higher inside the layer suggests that the grains are in an inertial state, thus collisional.

Hsu, Jenkins, and Liu [HJL04] proposed a model for the sheet flow transport and obtained an additional striking specificity of the concentration profile: a "shoulder" in the middle of the sheet flow layer, where the concentration is constant over a height of some grains diameters. Revil-Baudard [Rev14] mentions that this shoulder, which they note can be obtained from two different modelling approaches, may be smoothed out in their experiment data by their ensemble averaging and time averaging methods. Indeed, their results were averaged over 11 repetitions of the same run, and by the way they proved the results are actually very repeatable, suggesting strong determinism in the phenomenon.

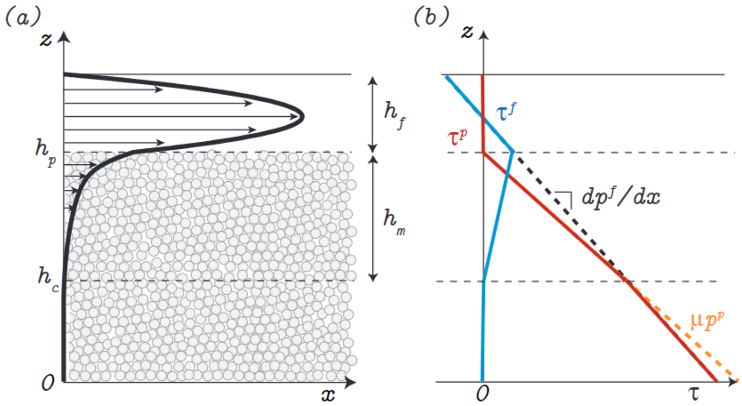

Figure 8: Sketch of the laminar sheet flow velocity and stress profiles upon which is based the two phase model of Ouriemi, Aussillous, and Guazzelli [OAG09]. Figure 4 in [Aus+13].

Ouriemi [Our07] and Aussillous et al. [Aus+13] investigated the sheet flow regime in laminar conditions. Ouriemi [Our07] developed a two phase model with a Coulomb rheology, thus obtaining an analytical solution, and ran experiments measuring the bed height evolution and fluid velocity profile in pipes. Aussillous et al. [Aus+13] ran flume experiments, providing profile details measurements to compare to Ouriemi's model but also two other rheological models including a $\mu(I)$ rheology. The comparisons include both scaling laws on integral quantities and velocity profiles. They confirmed (scarce) precedent studies findings that (i) there is no or very little slip velocity between the two phases and (ii) the concentration profile is mostly constant through the bed before dropping abruptly at the top of the sheet flow layer, over a height of only $\sim 2d$. The two phase model is thus based on a 4 region separation : (I) pure fluid, (II) (abrupt) transition region, (III) granular motion with constant porosity and (IV) granular bed at rest. The fluid velocity profile is obviously parabolic as expected, and the solid velocity profile is also parabolic from h_p to h_c where h_c is the limit between region III and IV with $\frac{du_p}{dy}(h_c) = 0$. See fig. 8, note region (II) is not directly visible. Kidanemariam and Uhlmann [KU14] validated these results with DNS-DEM simulation, which Vowinckel et al. [Vow+21] extended (still with DNS-DEM) an order of magnitude higher in Stokes and Shields numbers, leading to extreme cases of laminar sheet flow. Indeed in the latter, the bed becomes completely mobilised down to the boundary wall, which directly affects the solid velocity profile and reverses its curvature for very high forcing. We will develop in a later section that in our case this is something we want to avoid since it is probably a finite bed effect which is not representative of the reality of natural beds. It remains very relevant to industrial processes though, which use finite section pipes to transport immersed granular materials and slurries.

1.4 Objectives of this work

Now that we clarified the context, we will clarify the scope of this work. The first and foremost objective is to develop a numerical experiment using `migflow` that is able to reproduce the sheet flow phenomenon. Then, we will focus on what I will call the lower-level analysis of which the goal is to extract profiles similar to those described earlier. The most important profiles are the fluid and solid velocity, the concentration and the sediment flux density. To do that, Lagrangian and Eulerian data from respectively the grains and the fluid will need to be processed so that it can be combined and produce time and space averaged profiles. Finally, the last objective which I will call the upper-level analysis will be to develop *meaningful* parameter sweeps and run batches of experiments to explore the scaling behavior of the sheet flow regime. For that to be possible, we will need to investigate the evolution of our experiments in time, to assert the attainment of steady state in each case.

2 Experiment

In this section, we present the design and setup of the numerical experiments. First, we describe the atomic stand-alone experiment and its parametrisation. Second, we describe the upper-level design of the experiment batches used to investigate how the atomic experiment scales with respect to its parameters.

The aim of our numerical experiment is to reproduce and analyze the essential features of sheet-flow transport in a controlled and minimal configuration. We target a setup similar to laboratory flume experiments. Accordingly, we focus on one-dimensional statistics averaged over time and the transverse direction, i.e., time-averaged profiles.

Solver considerations

Because our 2D numerical solver employs drag correlations developed for 3D flows, we use the 2D solver to extract trends that we expect to be representative of real experiments with symmetric configurations that are essentially 2D problems, such as flumes. It should be kept in mind, however, that 2D disk-grain dynamics correspond to the dynamics of cylinders in 3D and will therefore differ from true 3D grain behavior. Furthermore, although turbulence in open-channel flows was discussed earlier, a 2D direct fluid solver cannot reproduce 3D turbulence; and as already noted, no turbulence model is used here. In fact, 2D and 3D turbulence show different characteristics, and the word turbulent from now on is thus to take with a grain of salt and solely indicates that the Reynolds number is high and that the shear stress balance is dominated by *mixing* stresses in the core of the flow as opposed to the Newtonian laminar term. At high Reynolds number however, for the purely 2D Navier-Stokes equations, the theoretical turbulent channel flow structure is still logarithmic (which follows from the fact that Millikan's argument does not depend on the number of dimensions) but the von Kàrmàn constant and the offset vary with Re_p, as investigated by L'vov, Procaccia, and Rudenko [LPR09]. The order of magnitude also remains similar and according to the latter paper results, the velocity profile obtained in the 3D case is a lower bound on the in the range of Re we are interested in. But in any case the mesh refinement we will use for the purpose of sheet flow experiments does not allow us to resolve the turbulence with sufficient fidelity. The lack of mesh refinement introduces numerical dissipation, drifting the numerical velocity profile towards the laminar profile more than it should be at the same Reynolds number. With these remarks in mind, we can expect the velocity profile obtained from the fluid solver without bed movement to sit between the 3D turbulent logarithmic profile and the laminar quadratic profile.

2.1 One experiment

The domain of the numerical experiment, represented on fig. 9, is a 2D box of height H and width L with a sediment bed of height h_p and tilted at an angle θ with respect to the horizontal. The height of the fluid part is noted h_f so that the total height of the system is $H = h_f + h_p$. The boundary conditions are as follows:

- The bottom boundary is a no-slip smooth wall: $u(0) = 0, v(0) = 0$
- The top boundary is a free-slip smooth wall: $\frac{du}{dy}(H) = 0, v(H) = 0$
- The left and right boundaries form a periodic boundary condition.

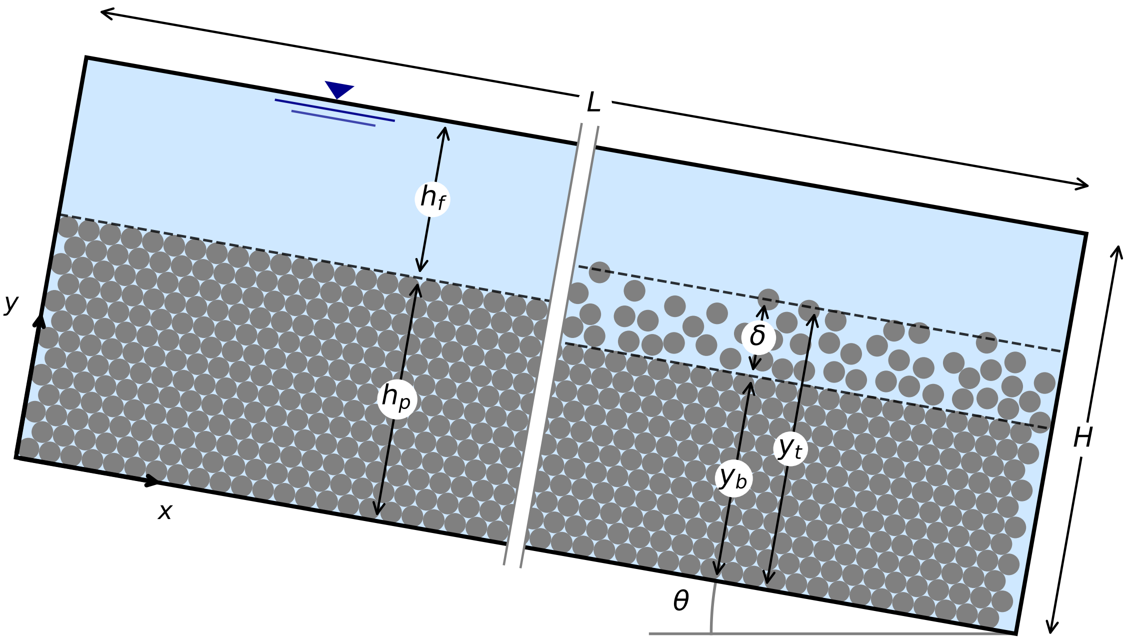

Figure 9: Domain of the numerical experiment and definitions of the initial and running geometric parameters. Left half: initial conditions. Right half: bed load transport. y_t is the height of the top of the mobile layer and y_b is the height of the fixed bed so that $\delta = y_t - y_b$ is the thickness of the mobile layer. The frame of reference with its origin are shown at the bottom left. The hexagonal packing is not representative of neither the reality nor the packings obtained via polydisperse numerical simulations.

Additionally, following the laboratory methodology of Revil-Baudard et al. [Rev+15], the bottom layer of grains will be allowed to be glued to the domain, mimicking an infinite bed under it which will prevent the bed to detach entirely and slide over the wall. It is clear caution will have to be taken to ensure the gradient of the fluid velocity is small at that place. If the gradient is non-negligible, it suggests that the bed depth is too small with respect to the dynamics of the problem, and we risk ending up non-representative of the phenomenon.

The definitions of the fixed bed height y_b and the top of the mobile layer height y_t vary by authors, and we use in this work the definitions of Capart and Fraccarollo [CF11]. y_t is commonly defined as the height above the maximum peak of the transport rate at which the concentration drops to $\phi = 0.08$, which in 3D is equivalent to require that the particle interdistance drops to roughly the grain diameter. The fixed bed height y_b is defined as the height below the maximum transport rate at which the granular strain rate $\frac{du_s}{dy}$ is equal to 2% of its maximum value.

$$y_t \quad \text{so that} \quad \phi(y_t) = 0.08 \tag{102}$$

$$y_b \quad \text{so that} \quad \frac{du_s}{dy}(y_b) = 0.02 \cdot \max\left(\frac{du_s}{dy}\right) \tag{103}$$

To be able to set the flow conditions of the transport in terms of Shields number and Re_p, we do not need to know what the velocity profile will develop to. Those numbers only depend on the external experiment parameters. It would be naive however to forget about the bulk Reynolds number as we would very easily encounter a situation where we imposed a large driving force on the fluid to match a large wall shield stress, but we would also end up with very large laminar bulk velocity and thus a large Reynolds number. The solver could very well still converge on the laminar velocity due to the several reasons cited above. In cases where the ratio between the fluid height and the grain diameter is small, this would lead to exaggerated drag on the mobilised particles. In the end we thus also need to constrain the bulk Reynolds number to avoid obtaining unrealistic situations. Note again that even if that constraint is approximate due to the several limitations, the constraints on Re_p and the Shields number, which are the most important in this case, remain accurate since they do not depend on the velocity profile.

Just for One experiment, we can easily compute by hand the adapted external parameters to match the three dimensionless numbers (τ^*, Re_p, Re) we need, but for A batch of experiments we will need to automatically match the external parameters to the swept dimensionless numbers, thus solve a nonlinear system of equations with piece wise definitions that are the laminar and turbulent cases.

The analytical relations of interest were obtained in section Laminar fluid flow over an inclined plane for the laminar case, and in section Turbulent fluid flow over an inclined plane for the turbulent case. To set those initial conditions, we will consider the bed, which is immobile at the start of each simulation, to be a rough wall and assume the obtained fluid height to be the height of a normal channel. At low Reynolds number, the laminar velocity profile can be reproduced exactly as will be validated later.

Knowing we need to use those relations before even running the simulations, we need to know the Reynolds number to be able chose between the laminar and turbulent equations. However, we do not know the bulk velocity a priori. Thus, we compute the Reynolds number associated with the laminar profile and verify that it is indeed low enough to use the laminar profile. If it is not, we compute the Reynolds number associated with the turbulent profile and verify that it is high enough to use the turbulent profile. In this way the Reynolds number will be constrained using the correct relations. For the sake of computational feasibility it was not possible to limit ourselves to purely laminar Reynolds numbers, though still not entering the fully developed turbulent regime. In fact, the Reynolds number computed from the turbulent profile is never verified to be high enough for that profile to exist in our simulations, meaning we are at most in the transitional regime.

Note also that while the flow is developing in the channel from the initial state, the bed can start mobilising. This means the actual flow conditions set by the monophase equations may not be reached at all, and this is especially true when the fluid flow height to grain diameter ratio is small. That also means the constrained Reynolds number from the above discussion is also an upper bound since it is considering no stress is carried by the granular media. The problem of getting to an equilibrium state will be discussed later.

2.2 A batch of experiments

2.2.1 Sweeping with care

Running batches of numerical experiments is not as straightforward as sweeping the parameters of the atomic experiment, especially when the span of the parameters is large and the phenomenon regimes are distinct.

The first culprit is computational time. In our case it scales with the following three parameters:

I **The number of grains** is determined by the bed surface $h_p \times L$ and the grain diameter d and scales roughly as $N_g \sim Lh_p/d^2$.

II **The number of mesh nodes** is determined by the bed length, total height $H = h_p + h_f$ and the grain diameter d, as we constrained the mesh element size to a fixed ratio with respect to the grain diameter. The number of nodes thus scales roughly as LH/d^2.

III **The number of time steps** has two components; the number of fluid time steps and the number of grain time steps, the latter being an order of magnitude larger than the former. It also obviously scales with the total time of the simulation, which in turns depends on the time it takes for the flow to reach a steady state, which is not known a priori. The number of time steps thus scales roughly as $N_t \sim T n_{sub}/dt$, where T is the total simulation time, dt is the fluid time step size and n_{sub} is the number of substeps for the grain solver.

The second culprit is the physical meaningfulness of every experiment resulting from parameter sweeps.

i **The bulk Reynolds number**, as mentioned earlier has to be constrained due to the limitations of the solver. It depends mostly on the fluid properties (μ, ρ), the height h_f, the driving force $\mathbf{F}$, and to a lesser extent on the grain diameter through the bed roughness. See eq. (31) and eq. (74) for the laminar and turbulent cases respectively.

ii **The fluid flow height** h_f must be large enough with respect to the grain diameter. The mobile layer thickness should not be capped by the fluid depth as that would distort the correlations with the other parameters. Studies show that the mobile layer thickness is of order of magnitude $\mathcal{O}(10d)$ [CF11; Rev+15]. Furthermore, we want to minimise contacts between the grains and the top wall, since a solid roof is probably not a good representation of a free surface with respect to the grains.

iii **The thickness of the bed** h_p, as mentioned as well, has to be large enough to allow the bed to develop a mobile layer, the bottom of which is not too close to the wall and the bed should not detach and slide as a block. It must also be large enough that the fluid velocity profile show a near zero derivative at the bottom $\frac{du}{dy}(y=0) \simeq 0$ since there should be no current deep inside a sediment bed. Those two requirement are related.

iv **The establishment of steady state** at the end of the simulation, so that we can extract meaningful correlations. Obviously, when we ask ourselves what the dimensionless transport rate is at some Shields and granular Reynolds number, we ask about the equilibrium mean transport rate and not the transient effects. The actual physical time is determined by the experiment parameters and is not known a priori. We will get back on this problem later.

One can directly see that there are conflicts between some requirements for the experiment to remain physically meaningful and the computational time. Hence, compromises will have to be found.

The bed length L is chosen so that the problem computational complexity is not prohibitive because of the size of the mesh and the number of grains, while still providing sufficient space for the longitudinal averaging of the flow and granular quantities. It must also be large enough with regard to the periodic boundary conditions, and we tried to maintain a horizontal aspect ratio $H/L < 1$. It was thus set as an experimenter choice and not motivated by a rigorous quantitative criterion. It is also fixed and not recomputed depending on the parameters of the experiment, which is also a choice.

From eqs. (31), (34), (69) and (74), the system of equations to fix the dimensionless numbers (τ^*, Re_p, Re) is:

$$Re_{lam} = \frac{\rho U h}{\mu} = \frac{\mathbf{F} h_f^3}{3\nu^2\rho} = u_\tau^2 \frac{h_f^2}{3\nu^2} \tag{104}$$

$$Re_{turb} = \frac{U h_f}{\nu} = u_\tau \frac{h_f}{\nu}\left(\frac{1}{\kappa}\left[\ln\left(\frac{h_f}{k_s}\right) - 1\right] + B(Re_p)\right) \tag{105}$$

$$\tau^* = \frac{\mathbf{F} h_f}{gd(\rho_s - \rho)} = \frac{u_\tau^2}{gd(\frac{\rho_s}{\rho} - 1)} \tag{106}$$

$$Re_p = Re_p = Re_{k_s} = \frac{u_\tau d}{\nu} = \frac{\sqrt{\tau_w/\rho}\, d}{\nu} = \frac{\sqrt{\mathbf{F} h_f}\, d}{\nu\sqrt{\rho}} \tag{107}$$

where $k_s = d$ is the grain diameter. The chosen set of unknowns are the driving force $\mathbf{F}$, the fluid height h_f, and the fluid kinematic viscosity ν. This allowed us to avoid tweaking the granular solver parameters or the domain length between experiments, which would probably have been necessary if the grain size had changed. From eq. (104) and eq. (107), we get:

$$h_f = \frac{\sqrt{3Re_l}\, d}{Re_p} \tag{108}$$

The fluid height h_f is computed to match the bulk Reynolds number Re_l. If the computed h_f falls outside the prescribed range $\left(\frac{h_f}{d}\right)_{\min} \le \frac{h_f}{d} \le \left(\frac{h_f}{d}\right)_{\max}$ (relative to the above discussion), it is clipped to the bounds and Re_l is recomputed. This reflects a compromise between solver-related fidelity (Re_l) and physical meaningfulness (bounds on h_f). From there, the kinematic viscosity and the driving force follow from the remaining equations, choosing laminar or turbulent profiles according to a single threshold $Re_{l,\text{th}}$ eqs. (104) and (105).

The mesh size l_m, the height of the sediment bed h_p and the time step dt are then set using rule-of-thumbs scaling determined from pre-run "sample" experiments in the parameter sweep range. These are preliminary runs designed to identify suitable parameter bounds and scaling rules before launching the full batch of experiments. The parameter n_{sub} is kept constant with the help of the fact that the grain size is constant.

Discussion on the threshold $Re_{l,th}$

Note that Re_l is defined using the laminar profile; hence the turbulent bulk Reynolds number Re_t obtained after switching can be smaller than $Re_{l,\text{th}}$. Indeed,

$$\frac{Re_l}{Re_t} = \frac{U_l}{U_t} = \frac{u_\tau^2 \dfrac{h_f}{3\nu}}{u_\tau\left[\dfrac{1}{\kappa}\left(\ln\dfrac{h_f}{d} - 1\right) + B_s\right]} = \frac{Re_\tau}{3\left[\dfrac{1}{\kappa}\left(\ln\dfrac{h_f}{d} - 1\right) + B_s\right]} \tag{109}$$

With $\kappa \simeq 0.41$ ($1/\kappa \simeq 2.44$), $B_s \in [5.5, 9.5]$ and $10 < \frac{h_f}{d} < 100$, monotonicity in both arguments gives

$$\left[\tfrac{1}{\kappa}\big(\ln 10 - 1\big) + 5.5\right] \le \underbrace{\tfrac{u_{max}}{u_\tau}}_{u^+_{max}} \le \left[\tfrac{1}{\kappa}\big(\ln 100 - 1\big) + 9.5\right]$$

i.e. numerically $u^+_{max} \in [\,8.7,\, 18.3\,]$. Hence

$$26\,\frac{Re_l}{Re_\tau} < Re_t \;<\; 55\,\frac{Re_l}{Re_\tau} \tag{110}$$

$$\Big\downarrow Re_l = \tfrac{1}{3}Re_\tau^2 \iff Re_\tau = \sqrt{3\,Re_l} \tag{111}$$

$$15\,\sqrt{Re_l} < Re_t \;<\; 32\,\sqrt{Re_l}\,. \tag{112}$$

We have $x = 15\sqrt{x}$ at $x = 225$ and $x = 32\sqrt{x}$ at $x = 1024$. Thus, for $Re_l \gtrsim 10^3$, one has $Re_t < Re_l$ for all $10 < \frac{h_f}{d} < 100$ and $B(Re_p) \in [5.5, 9.5]$. Accordingly, we set $Re_{l,\mathrm{th}} = 10^3$, which falls within the classic open-channel transition range [Yal77] and is consistent with the above laminar–turbulent mapping. A higher threshold could be justified. For example, the value $Re_t \approx 2000$ is often cited and is attained by the two bounds at respectively $Re_l \approx 4000$ and $Re_l \approx 18000$. Add to this the numerical dissipation that also pushes the transition back. However, rigorously refining $Re_{l,\mathrm{th}}$ would require quantifying numerical dissipation and invoking transition theory, both beyond our scope. Finally, note that even if the above analysis is based on approximate grounds, it will only affect the constraint on the bulk Reynolds number which has been set to mitigate the solver limitations, while it will not affect the constraints on τ^* and Re_p.

2.2.2 Experiment parameters

At first, the parameter sweeps were supposed to be run on a HPC cluster. However, for design purposes, the sweeps were firstly limited to 36 variations so that they can be run on the machine of the author. Due to the amount of work necessary to automate parameter sweeping, simulation batch running and batch post-processing along with rigorous code and data versioning, the parameter sweeps were not adapted to run on an HPC cluster. The computational complexity was chosen empirically so that a single threaded run can be finished in less than 24 hours on an AMD Ryzen 7950x CPU, so that a batch of 36 runs takes less than 2 days to run.

However, 36 variations will already allow us to make some relevant observations. The numerical values of the parameters are given in table 1, and we remind that we set $(\mu, \mathbf{F}, h_f)$ for the targets (τ^*, Re_p, Re_l) and the other parameters are derived from those. Exceptions are (h_p, dt, n_{sub}) that were adapted with rule of thumbs formulas to try to keep each experiment meaningful according to the above discussion. The given Reynolds number Re is the theoretical one derived from either the log law or the Poiseuille law, chosen according to the above threshold of 1000. It was kept as small as possible while maintaining a minimum ratio $h_f/d > 12$. The case names are simply related to the 6 unique Shields and Re_p values swept. One variable that is not possible to observe precisely with such a low density of variations, and that was not in the scope of this work, is the critical Shields number τ^*_c.

Table 1: Experiment parameter sweeps

case	τ^*	Re_p	Re	h_f [cm]	μ [mPa · s]	$\mathbf{F}$ [Pa/m]	h_p [cm]	$g_{f,x}$ [m/s^2]	τ_w [Pa]	u_τ [m/s]	dt [s]	n_{sub}
Rp1Sh1	0.0631	0.1	33.3	30	566	-1.19	11	-0.0479	0.357	0.0189	0.003	8
Rp1Sh2	0.151	0.1	33.3	30	877	-2.85	11	-0.0462	0.855	0.0292	0.003	8
Rp1Sh3	0.363	0.1	33.3	30	1.36e+03	-6.84	11	-0.0422	2.05	0.0453	0.003	8
Rp1Sh4	0.871	0.1	33.3	30	2.1e+03	-16.4	14.3	-0.0326	4.92	0.0702	0.003	8
Rp1Sh5	2.09	0.1	33.3	30	3.26e+03	-39.4	19.8	-0.0097	11.8	0.109	0.003	8
Rp1Sh6	5.01	0.1	33.3	30	5.05e+03	-94.4	19.8	0.0453	28.3	0.168	0.003	8
Rp2Sh1	0.0631	0.398	200	18.5	142	-1.93	11	-0.0471	0.357	0.0189	0.003	8
Rp2Sh2	0.151	0.398	200	18.5	220	-4.63	11	-0.0444	0.855	0.0292	0.003	8
Rp2Sh3	0.363	0.398	200	18.5	341	-11.1	11	-0.0379	2.05	0.0453	0.003	8
Rp2Sh4	0.871	0.398	200	18.5	529	-26.7	14.3	-0.0224	4.92	0.0702	0.003	8
Rp2Sh5	2.09	0.398	200	18.5	819	-64	19.8	0.0149	11.8	0.109	0.003	8
Rp2Sh6	5.01	0.398	200	18.5	1.27e+03	-153	19.8	0.104	28.3	0.168	0.003	8
Rp3Sh1	0.0631	1.58	200	4.64	35.7	-7.69	11	-0.0414	0.357	0.0189	0.003	8
Rp3Sh2	0.151	1.58	200	4.64	55.4	-18.4	11	-0.0306	0.855	0.0292	0.003	8
Rp3Sh3	0.363	1.58	200	4.64	85.7	-44.2	11	-0.0048	2.05	0.0453	0.003	8
Rp3Sh4	0.871	1.58	200	4.64	133	-106	14.3	0.0571	4.92	0.0702	0.003	8
Rp3Sh5	2.09	1.58	200	4.64	206	-255	19.8	0.206	11.8	0.109	0.003	8
Rp3Sh6	5.01	1.58	200	4.64	319	-611	19.8	0.562	28.3	0.168	0.003	8
Rp4Sh1	0.0631	6.31	1.02e+03	3.6	8.98	-9.9	11	-0.0391	0.357	0.0189	0.002	8
Rp4Sh2	0.151	6.31	1.02e+03	3.6	13.9	-23.8	11	-0.0253	0.855	0.0292	0.002	8
Rp4Sh3	0.363	6.31	1.02e+03	3.6	21.5	-57	11	0.00794	2.05	0.0453	0.002	8
Rp4Sh4	0.871	6.31	1.02e+03	3.6	33.4	-137	14.3	0.0877	4.92	0.0702	0.002	8
Rp4Sh5	2.09	6.31	1.02e+03	3.6	51.7	-328	19.8	0.279	11.8	0.109	0.002	8
Rp4Sh6	5.01	6.31	1.02e+03	3.6	80	-787	19.8	0.738	28.3	0.168	0.002	8
Rp5Sh1	0.0631	25.1	4.13e+03	3.6	2.26	-9.9	11	-0.0391	0.357	0.0189	0.002	8
Rp5Sh2	0.151	25.1	4.13e+03	3.6	3.49	-23.8	11	-0.0253	0.855	0.0292	0.002	8
Rp5Sh3	0.363	25.1	4.13e+03	3.6	5.41	-57	11	0.00794	2.05	0.0453	0.002	8
Rp5Sh4	0.871	25.1	4.13e+03	3.6	8.38	-137	14.3	0.0877	4.92	0.0702	0.002	8
Rp5Sh5	2.09	25.1	4.13e+03	3.6	13	-328	19.8	0.279	11.8	0.109	0.002	8
Rp5Sh6	5.01	25.1	4.13e+03	3.6	20.1	-787	19.8	0.738	28.3	0.168	0.002	8
Rp6Sh1	0.0631	100	1.55e+04	3.6	0.566	-9.9	11	-0.0391	0.357	0.0189	0.001	8
Rp6Sh2	0.151	100	1.55e+04	3.6	0.877	-23.8	11	-0.0253	0.855	0.0292	0.001	8
Rp6Sh3	0.363	100	1.55e+04	3.6	1.36	-57	11	0.00794	2.05	0.0453	0.001	8
Rp6Sh4	0.871	100	1.55e+04	3.6	2.1	-137	14.3	0.0877	4.92	0.0702	0.001	8
Rp6Sh5	2.09	100	1.55e+04	3.6	3.26	-328	19.8	0.279	11.8	0.109	0.0005	10
Rp6Sh6	5.01	100	1.55e+04	3.6	5.05	-787	19.8	0.738	28.3	0.168	0.0005	10

3 Results

3.1 One experiment

3.1.1 Profiles

The first profiles we will present are obtained in the fully laminar regime (both numerically and physically), case Rp1Sh4, above the common sheet flow threshold of $\tau^* = 0.5$ on fig. 10. As a reminder of eq. (103) and eq. (102), Capart [CF11] define the top of the mobile layer y_t as the height above which the concentration drops to $\phi = 0.08$, dash-dotted line on plot, and the fixed bed height y_b as the height below which the solid shear rate $\frac{du_s}{dy}$ is equal to 2% of its maximum value, dashed line on plot. The y_k correspond to the height of the middle of the corresponding bin k. Binning is necessary to convert the grain Lagrangian data to Eulerian data so that it can be accumulated into profiles. The binning in this work is area-weighted, meaning we compute the intersections between a bin and all the grains (disks) contained in it to average the corresponding grain Lagrangian field. The y_i correspond to the heights of the horizontal lines over which the fluid field is averaged, by computing and averaging the exact interpolation values at the intersections between each line and every mesh element it crosses. The y_i are thus not necessarily the same as the y_k.

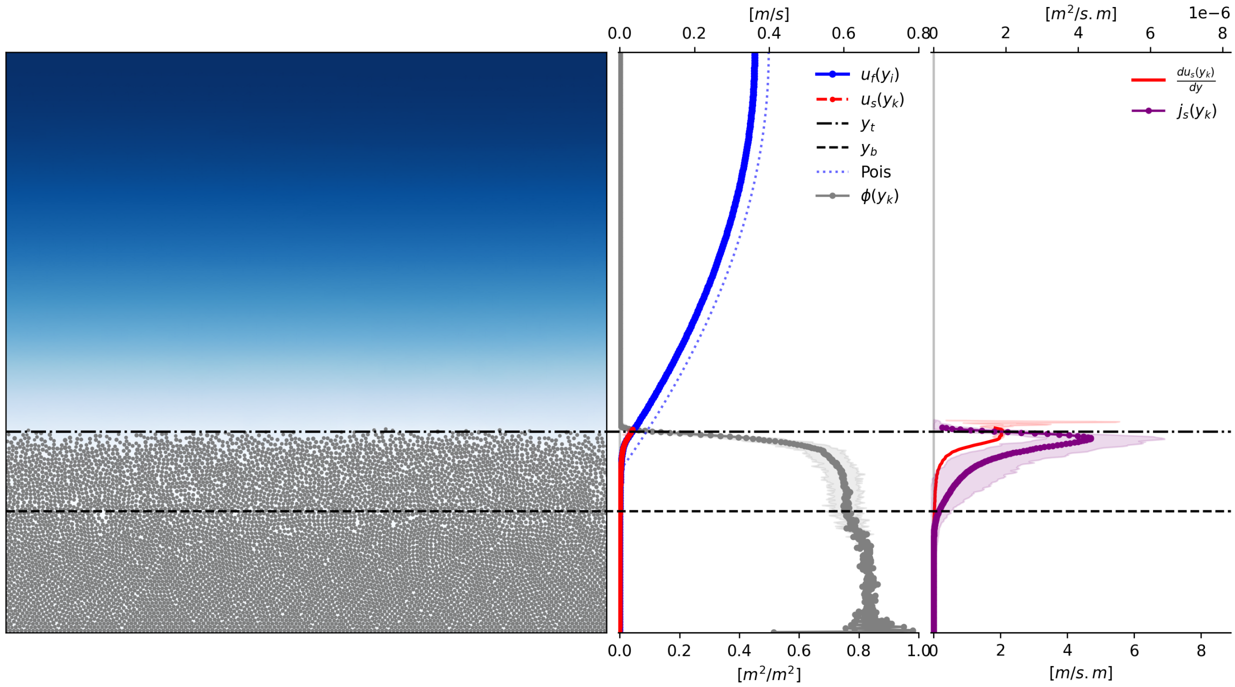

Figure 10: Profiles of the sheet flow experiment corresponding to case Rp1Sh4. On the left, the 2D velocity field and the grains. The dashed and dash-dotted lines indicate the limits of the mobile layer according to [CF11]. In the middle, the fluid u_f and solid u_s velocity profiles, along with the concentration ϕ profile. On the right, the sediment volumetric transport rate density j_s along with the solid shear rate $\frac{du_s}{dy}$. For every curve, the shaded area represents the extreme values during the time averaging period of 100s.

The first observation is that, in agreement with the literature, the concentration inside the mobile layer stays relatively constant and close to the packing concentration of the below bed. However, one could argue that the difference between the mobile layer concentration and the packing concentration constitutes an observation of the "shoulder" we introduced earlier. Either way, the concentration drop is in fact abrupt and located at the top of the mobile layer, as observed in laminar experiments. Accordingly, the flux density j_s shows a peak value high in the mobile layer, before falling abruptly too, contrasting with Revil-Baudard's results on fig. 7b. It is also observed that the slip between the fluid and the solid is very small and the fluid velocity profile is quadratic, as expected.

There is an offset between the theoretical solid-wall laminar profile (noted *Pois* on fig. 7b) as we chose the middle of the mobile layer as a virtual wall rather arbitrarily. The shape of the solid velocity profile is also very similar to fig. 8 by Aussillous et al. [Aus+13].

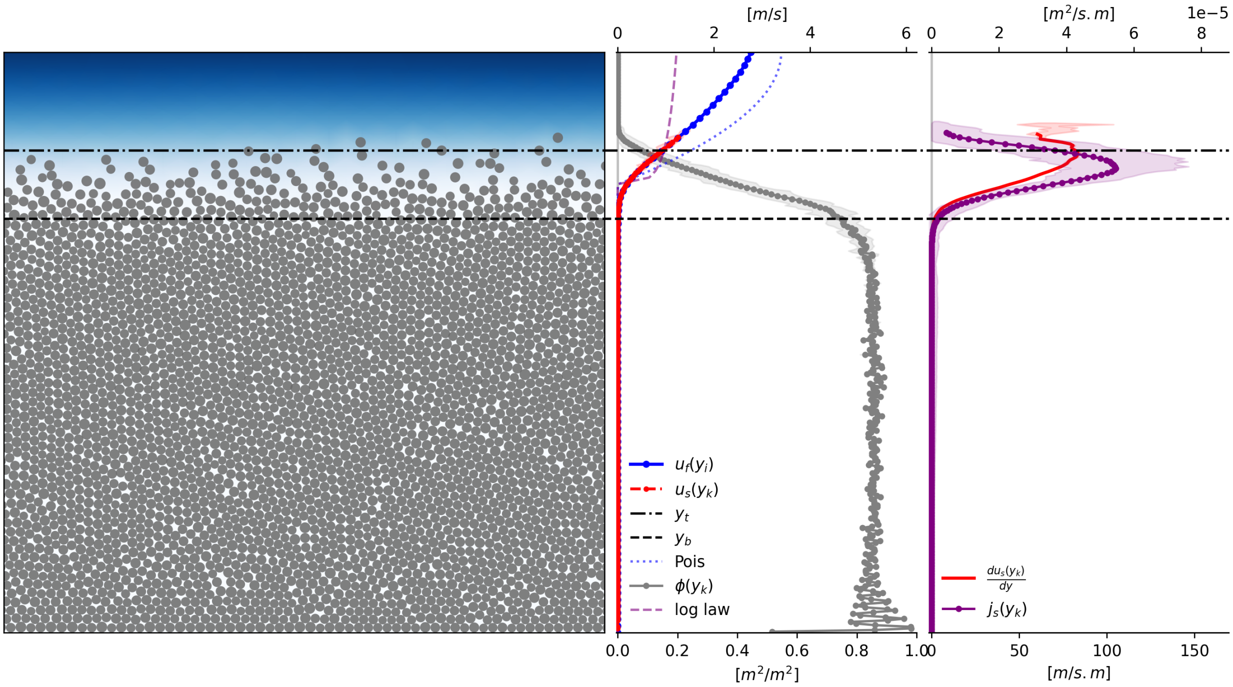

Figure 11: Profiles of the sheet flow experiment corresponding to case Rp4Sh4.

On fig. 11 we present the result for the case Rp4Sh4, which is the same as Rp1Sh4 but with a larger Shields number. One can observe the concentration and the velocity profiles present a more obvious linear region. In fact, the concentration now transitions over the whole mobile layer. This would need verification however since the mobile layer in this case is also smaller due to the fact h_f has to be decreased when increasing Re_p, so that the bulk Reynolds number Re does not explode. The flux density profile is also much more centered and symmetric than in fig. 10.

For an even higher particle Reynolds number Re_p as in fig. 12, we can start observing transient effects and an unstable bed. In this case as well as in Rp6Sh4, waves have developed and a periodic equilibrium has been attained, as demonstrated by the later time series of the same cases. The scatter in time samples, as represented by the shaded areas, is larger and this is especially true for the transport flux density. The fluid velocity profile is also very "dampened", attaining the log law order of magnitude while not being in truly turbulent conditions. The transport flux density profile also attests actual suspension transport, not so much present in precedent cases. Apart from sediment waves, moving "dunes" can also

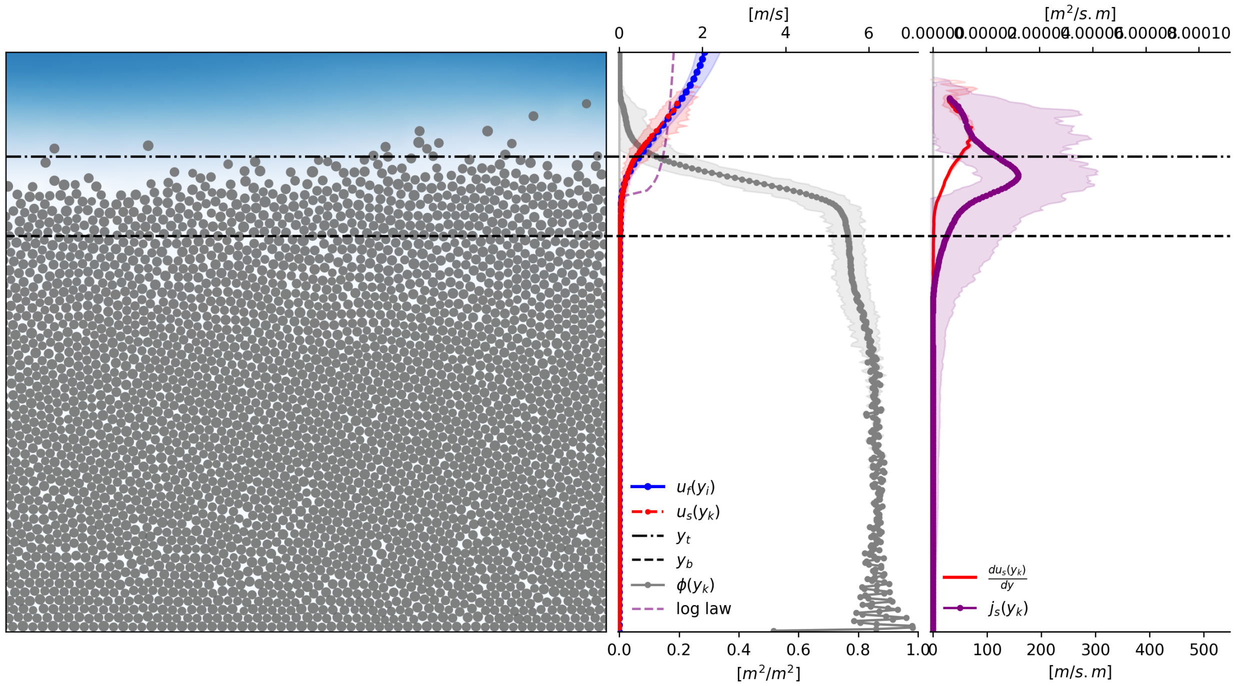

Figure 12: Profiles of the sheet flow experiment corresponding to case Rp5Sh4.

be observed as in the case Rp5Sh2 on fig. 13, which is expected since the Shields number is closer to the threshold of sheet flow, which is sometimes defined as the threshold at which the bed forms (dunes) are washed away by this new mobile layer.

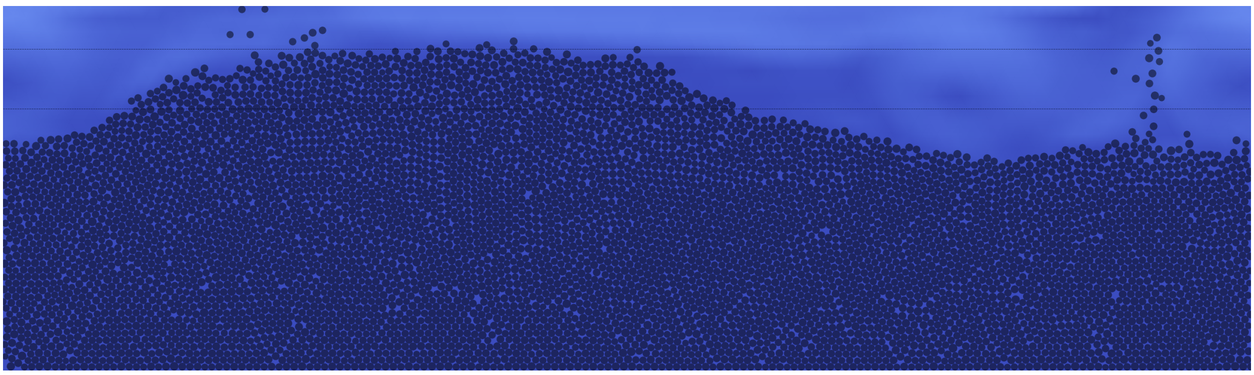

Figure 13: Formation of a dune in the case Rp5Sh2, close to the sheet flow Shields number threshold.

3.1.2 Time series

The time series of the mobile layer thickness δ and the dimensionless sediment transport rate q_s^* are shown on figures figs. 14 to 17. For each time series, a filtered curve with an exponential kernel is overlaid over the raw data (low opacity). The waves are clearly visible on the Rp5Sh4 case fig. 16. The formation of the dune then its creeping is also visible on the Rp5Sh2 case fig. 17.

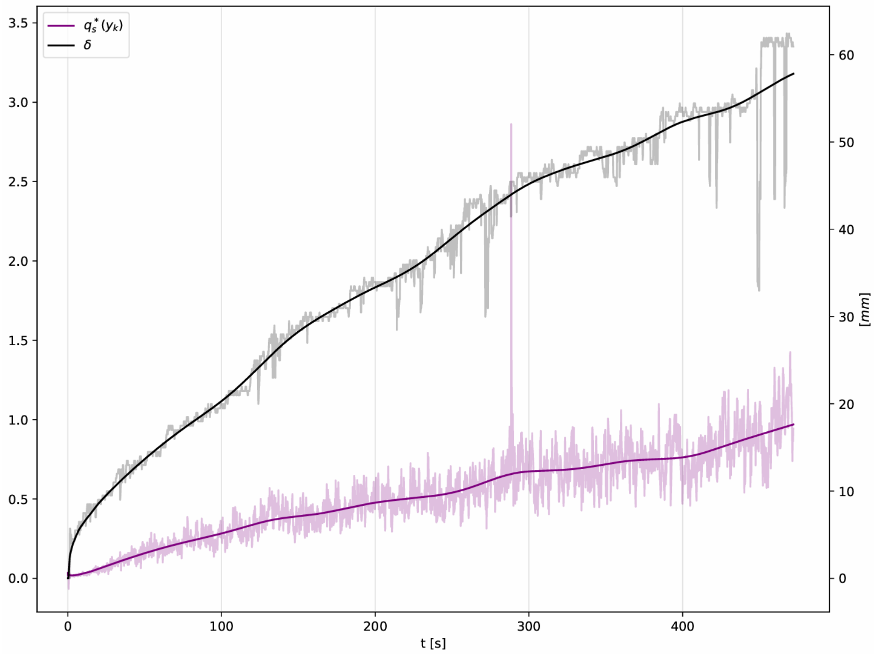

Figure 14: Time series of the sheet flow experiment corresponding to case Rp1Sh4. This case did not reach steady-state.

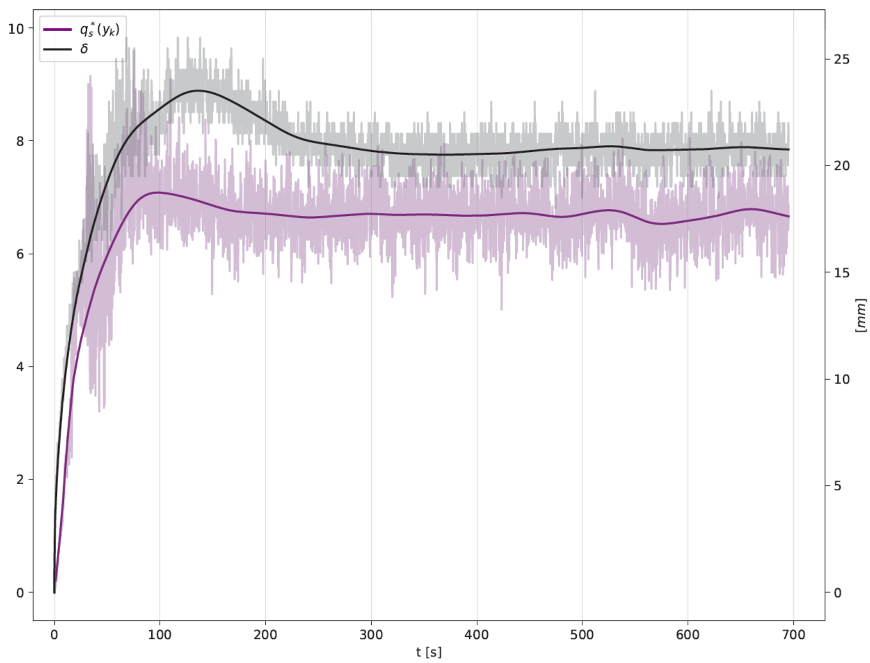

Figure 15: Time series of the sheet flow experiment corresponding to case Rp4Sh4.

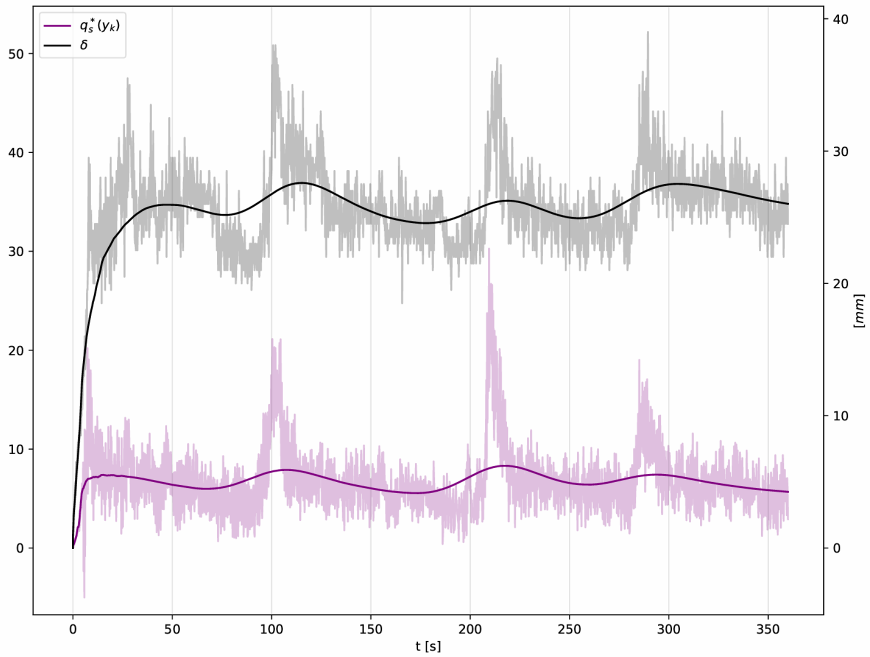

Figure 16: Time series of the sheet flow experiment corresponding to case Rp5Sh4.

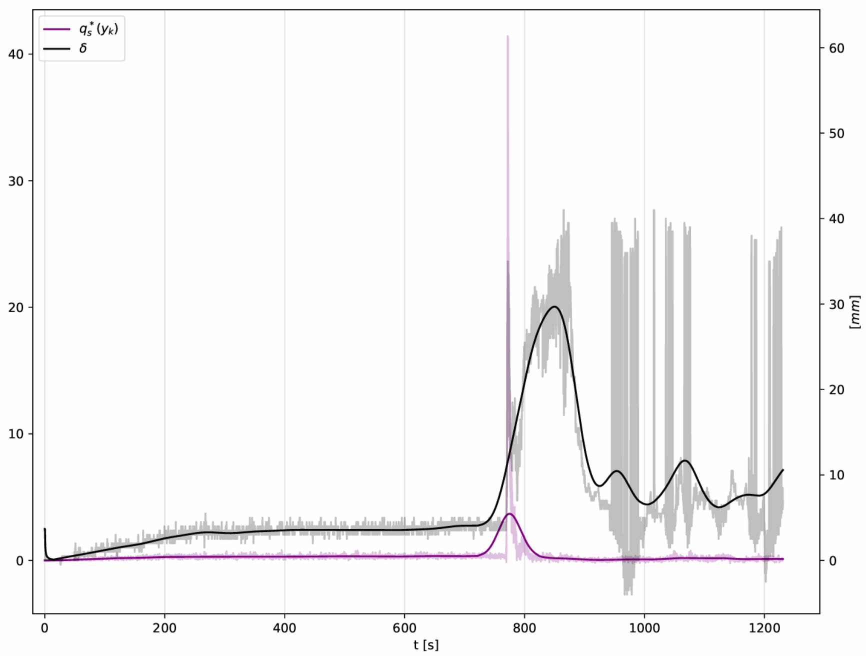

Figure 17: Time series of the sheet flow experiment corresponding to case Rp5Sh2.

3.2 A batch of experiments

A big part of the work for running batches of experiments has been diagnostics for the physical meaningfulness. Indeed, in the following figures sometimes are indicated the experiments that ended up in a "non-representative" state, relative to our earlier discussions.

3.2.1 Scaling laws

On fig. 18 we plot the dimensionless sediment transport rate q_s^* as a function of the Shields number τ^* for all the successful experiments. It can be seen that the scaling of the sediment flux with the Shields number is roughly cubic, even in Einstein form as it is here. It does seem to be lower for the higher Re_p (brown and purple curves), roughly quadratic.

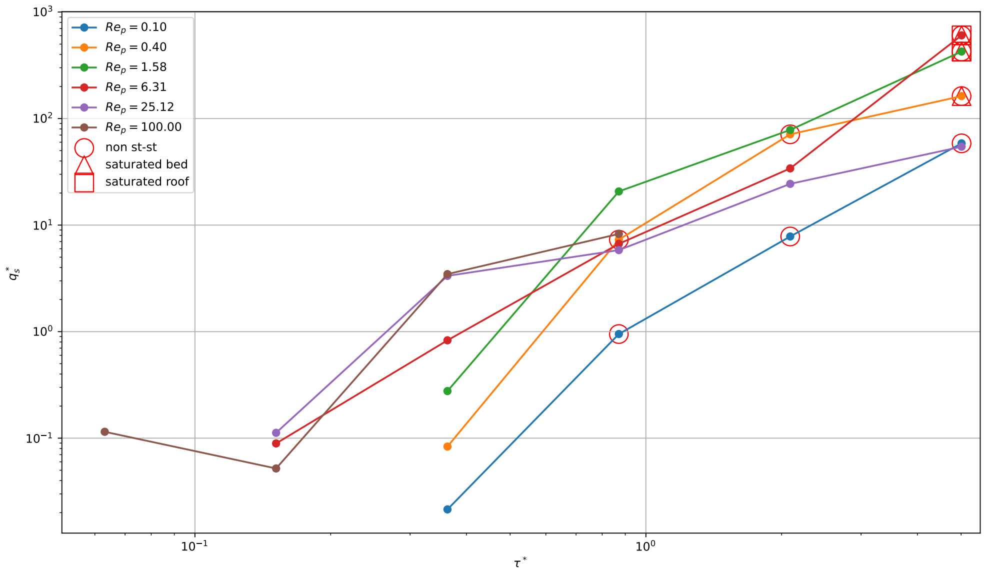

Figure 18: Dimensionless sediment transport rate q_s^* as a function of the Shields number τ^* for all the successful experiments.

On fig. 19 we plot the mobile bed thickness $\delta = y_t - y_b$ as a function of the Shields number τ^* for all the successful experiments. It appears that the bed thickness grows roughly linearly with the Shields number, which is in agreement with the literature.

3.2.2 Steady state identification

As stated in the section Sweeping with care, the establishment of steady state in each experiment run is crucial for the analysis of correlations between the parameters and the results. Since the time to steady state t_{ss} is not known a priori, procedural methods are used to identify it. The goal is that the simulation runs automatically stop when steady state is reached, but we will first develop the necessary procedures in post-processing. The parameters of interest are the fluid flow rate q, the sediment mobile layer thickness δ and the (dimensionless) sediment transport rate q_s^*. Those metrics could very well not reach steady state at the same time.

Since steady-state detection simply involves finding a plateau in our case, we are mostly interested in the time derivatives of the time series. However, the time series are very noisy

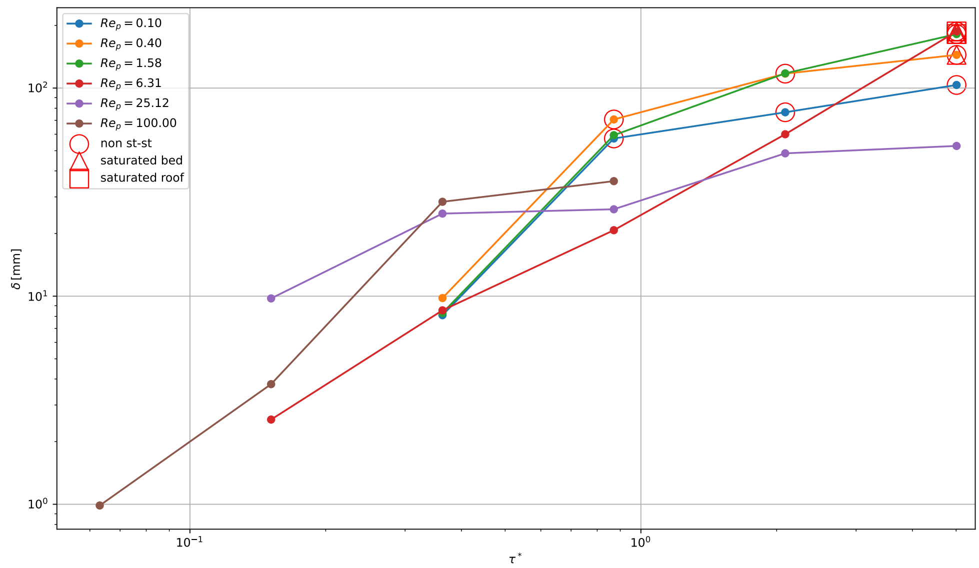

Figure 19: Mobile bed thickness δ as a function of the Shields number τ^* for all the successful experiments.

and thus need to be either filtered or smoothed. A plethora of different numerical filtering methods exist and a lot of them have been tested on the data for this work. Some of these filter can only be used in post-processing and are called non-causal or offline filters.

The method that yielded the best results is to fit an exponential model to the time series then apply a thresholding method on the derivative of the fitted curve. Let's denote our time serie variable $f(t)$. The natural parameters to fit a time series that comes from a state (pleateau) to get to another stable state (another pleateau) are:

- f_l the value of the left asymptote, corresponding to the initial state,
- f_r the value of the right asymptote, corresponding to the final state,
- $\Delta f = f_r - f_l$ the difference between the two asymptotes,
- t_d the time delay at which the inflection point occurs,
- τ the time constant which quantifies the rate at which an asymptote is reached.

The simplest model is the capacitor charge curve:

$$m(t) = \Delta f \left(1 - e^{-\frac{t-t_d}{\tau}}\right) + f_l \tag{113}$$

This model already gave more reliable performance than most filtering methods. However, it assumes that the start of the "charge" is a finite time t_d with a "current" spike at t_d, which is not always observed in our data. A better model would allow to have both an exponential growth from the first asymptote and an exponential decay to the second asymptote, such that the two "knees" are smooth. After some research, the author found no such common model. The most similar model is Richards' curve [Ric59] which is also called the generalised logistic function:

$$m(t) = \Delta f \frac{1}{\left(1 + e^{-\frac{(t-t_d)}{\tau}}\right)^{\frac{1}{\nu}}} + f_l \tag{114}$$

However, even if the parameter ν controls the asymmetry, this model does not allow for true decoupled curvature in the two knees, which is often observed in our data. Indeed, some series fit very well with the capacitor discharge curve which means the curvature at the first knee is very large while the curvature at the second knee is much smaller.

We model each time series $f(t)$ by a *tangent exponential* profile that transitions smoothly from a left plateau a_l to a right plateau a_r, with potentially different approach rates on each side. The model is

$$m(t) = \begin{cases} f_l + b_l \, \exp\big((t - t_d)/\tau_l\big), & t < t_d, \\ f_r + b_r \, \exp\big(-(t - t_d)/\tau_r\big), & t \geq t_d, \end{cases} \tag{115}$$

where $\tau_l, \tau_r > 0$ are time constants and t_d is the inflection/transition time. Note that $b_l > 0$ and $b_r < 0$. We enforce both continuity and tangency at t_d:

$$\text{(i) } f_l + b_l \; = \; f_r + b_r, \qquad \text{(ii) } \frac{b_l}{\tau_l} \; = \; -\frac{b_r}{\tau_r}. \tag{116}$$

Solving for b_l, b_r gives the closed forms:

$$b_l \; = \; \frac{f_r - f_l}{1 + \tau_r/\tau_l}, \qquad b_r \; = \; -\frac{\tau_r}{\tau_l} \, b_l. \tag{117}$$

This is the model that gave the best results in practice. It is simple, and the 5 parameters $(f_l, f_r, \tau_l, \tau_r, t_d)$ are directly interpretable.

To fit each model, several methods were also tested. Basic least square and RANSAC were found to be inadapted. We used instead `scipy.optimize` constrained optimisation functions with Powell's method and differential evolution. A simple initial guess procedure and a loss function were defined for each model. The loss functions are based on the mean square error and penalty terms to drive the solution away from the model parameters bounds. The initial guess strategy works as follows:

$$f_l = \langle f(t) \rangle_{t \in [0, 10dt]}, \quad f_r = \langle f(t) \rangle_{t \in [T - 10dt, T]}, \quad \tau_l = \frac{T}{500}, \quad \tau_r = \frac{T}{5}, \quad t_d = 0.8 \, t_{\text{start}} \tag{118}$$

where $T = t_{\max} - t_{\min}$ and t_{start} is a coarse change-point detected by thresholding. The chosen solution is then taken as the best fit among the initial guess and the solutions found by the optimisation methods.

The fits of the 34 successful experiments are shown on figs. 20 to 22.

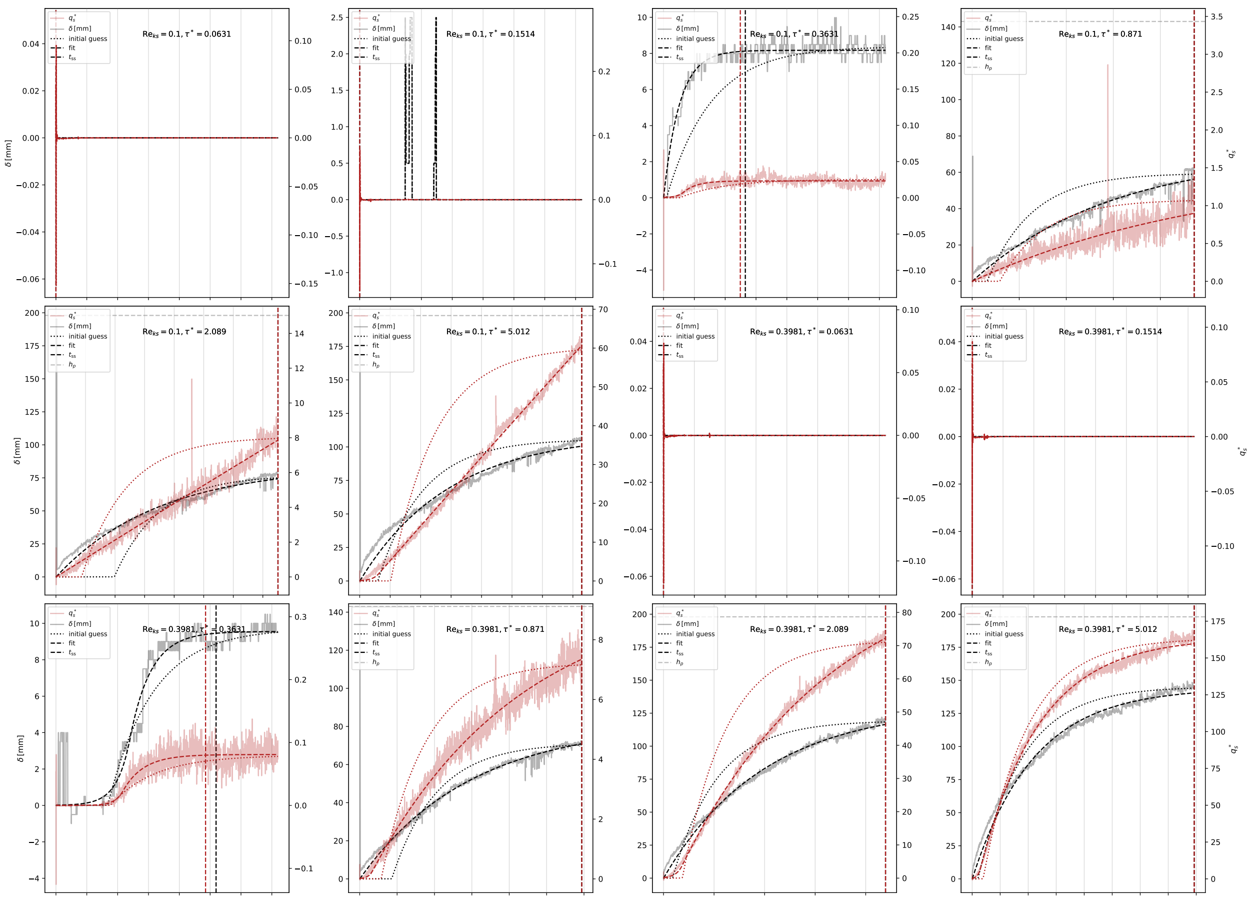

Figure 20: Fits of the steady-state identification double exponential model.

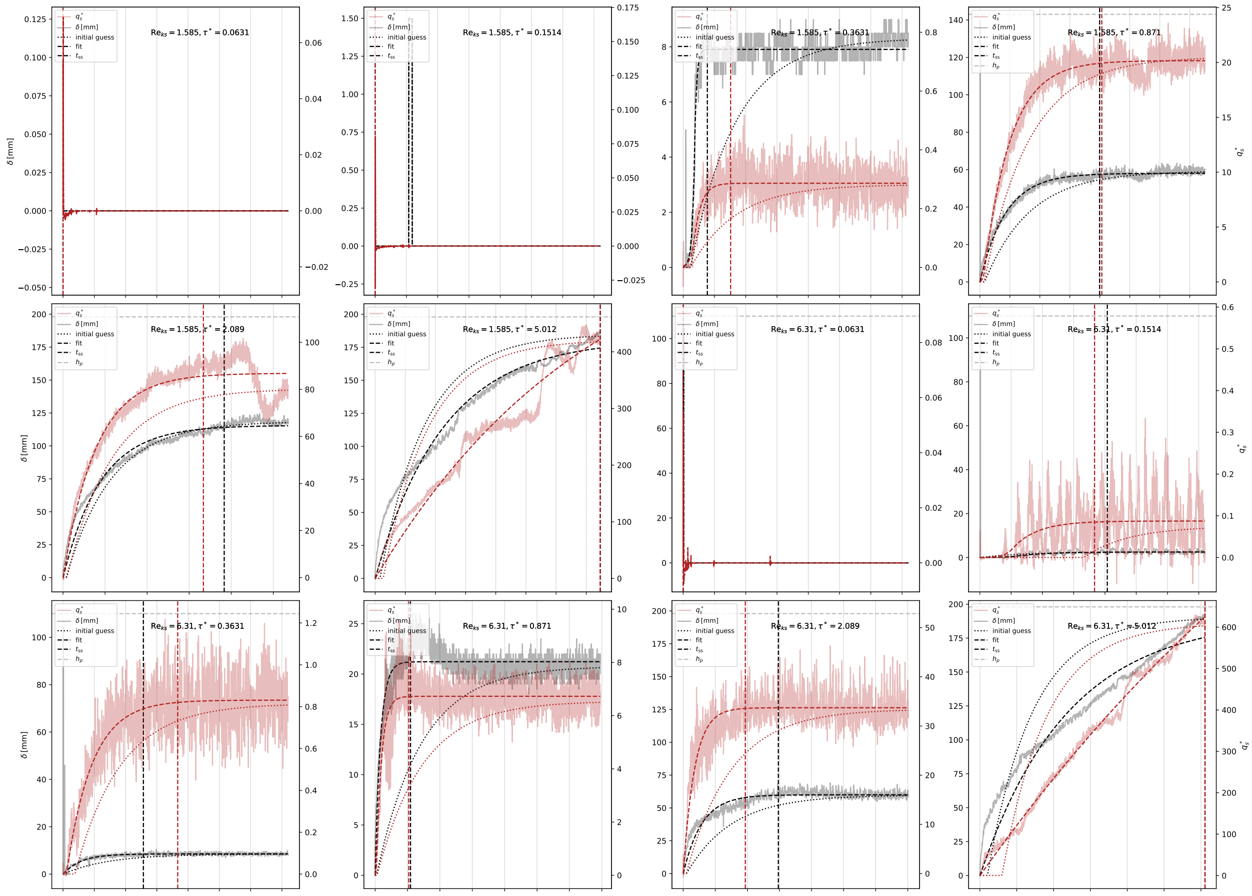

Figure 21: Fits of the steady-state identification double exponential model.

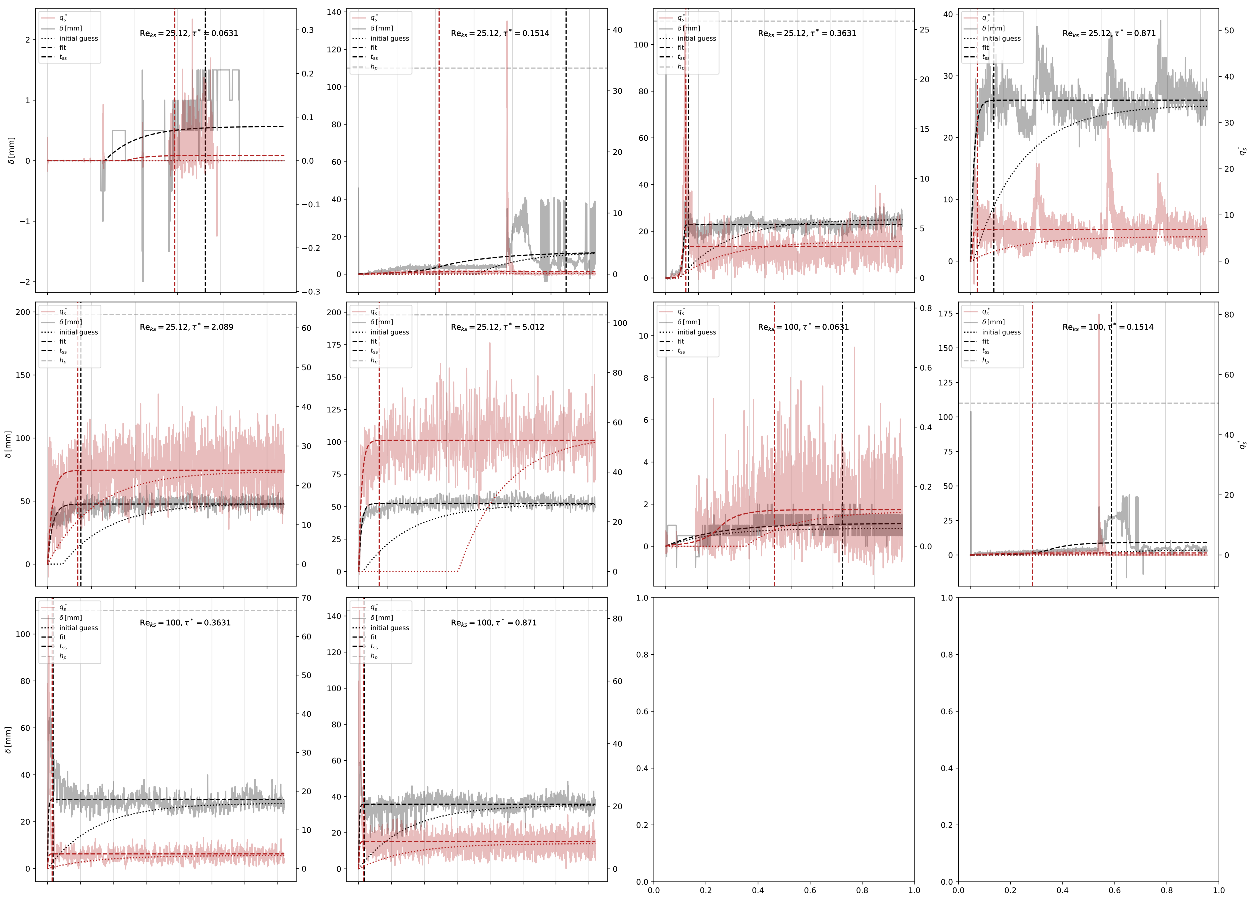

Figure 22: Fits of the steady-state identification double exponential model.

Conclusion

To conclude this work, we have developed a set of numerical experiments to study the transport of granular particles in a fluid flow in the form of sheet flow. We have shown that the numerical model is able to reproduce the main features of sheet flow transport both in terms of profiles and scaling laws. The results of the numerical experiments have been compared with experimental data from the literature, showing good qualitative agreement considering the limitations of the unresolved 2D model. The major part of the work done in thesis has been on the code to produce this parametric numerical experiment, and the potential for further analysis and development is crucially significant. This is due mostly to the fact that the first objective was to develop a working numerical experiment, and a true state of the art as well as the analyses came after, leading to this modest report. The results are however promising and show that the numerical experiment setup is totally capable of reproducing sheet flow sediment transport phenomena.

Disclaimer : The use of artificial intelligence tools, such as ChatGPT, has been limited to the generation of simple code and paraphrasing of text.

References

[Aus+13] Pascale Aussillous et al. "Investigation of the mobile granular layer in bedload transport by laminar shearing flows". In: *Journal of Fluid Mechanics* 736 (2013), pp. 594–615. DOI: 10.1017/jfm.2013.546.

[Bag54] Ralph A. Bagnold. "Experiments on a Gravity-Free Dispersion of Large Solid Spheres in a Newtonian Fluid under Shear". In: *Proceedings of the Royal Society of London A* 225 (1954), pp. 49–63. DOI: 10.1098/rspa.1954.0186.

[Bag56] R. A. Bagnold. "The Flow of Cohesionless Grains in Fluids". In: *Philosophical Transactions of the Royal Society of London. Series A, Mathematical and Physical Sciences* 249.964 (1956), pp. 235–297. DOI: 10.1098/rsta.1956.0020.

[CF11] Hervé Capart and Luigi Fraccarollo. "Transport layer structure in intense bedload". In: *Geophysical Research Letters* 38.20 (Oct. 2011), p. L20402. DOI: 10.1029/2011GL049408.

[CGU11] C. Chan-Braun, M. García-Villalba, and M. Uhlmann. "Force and torque acting on particles in a transitionally rough open channel flow". In: *arXiv preprint arXiv:1108.5924* (2011). URL: http://arxiv.org/abs/1108.5924.

[Cha04] Hubert Chanson. *The Hydraulics of Open Channel Flow*. 2nd ed. Chichester: John Wiley & Sons, 2004.

[Col56] D. Coles. "The law of the wake in the turbulent boundary layer". In: *Journal of Fluid Mechanics* 1.2 (July 1956), pp. 191–226. DOI: 10.1017/S0022112056000135.

[Con+19] Matthieu Constant et al. "Implementation of an unresolved stabilised FEM–DEM model to solve immersed granular flows". In: *Computational Particle Mechanics* 6.2 (2019). Published online 29 Sep 2018, pp. 213–226. DOI: 10.1007/s40571-018-0209-4. URL: https://link.springer.com/article/10.1007/s40571-018-0209-4.

[Dav15] Peter A. Davidson. *Turbulence: An Introduction for Scientists and Engineers*. 2nd ed. Oxford: Oxford University Press, 2015.

[Dey24] Subhasish Dey. *Fluvial Hydrodynamics: Hydrodynamic and Sediment Transport Phenomena*. 2nd ed. GeoPlanet: Earth and Planetary Sciences. Cham: Springer, 2024. ISBN: 978-3-031-26037-7. DOI: 10.1007/978-3-031-26038-4.

[Ein50] Hans Albert Einstein. *The Bed-Load Function for Sediment Transportation in Open Channel Flows*. Tech. rep. Technical Bulletin 1026. Washington, D.C.: U.S. Department of Agriculture, 1950. DOI: 10.22004/ag.econ.156389. URL: https://ageconsearch.umn.edu/record/156389.

[Hen+25] Michel Henry et al. "Multiscale FEM-DEM model for spontaneous droplet digging in a hot granular bed". In: *International Journal of Heat and Mass Transfer* 241 (2025), p. 126755. ISSN: 0017-9310. DOI: https://doi.org/10.1016/j.ijheatmasstransfer.2025.126755. URL: https://www.sciencedirect.com/science/article/pii/S0017931025000961.

[HJL04] Tian-Jian Hsu, James T. Jenkins, and Philip L.-F. Liu. "On two-phase sediment transport: sheet flow of massive particles". In: *Proceedings of the Royal Society A: Mathematical, Physical and Engineering Sciences* 460.2048 (2004), pp. 2223–2250. DOI: 10.1098/rspa.2003.1273. URL: https://doi.org/10.1098/rspa.2003.1273.

[Kar+23] Shashank K. Karra et al. "Pore-resolved investigation of turbulent open channel flow over a randomly packed permeable sediment bed". In: *Journal of Fluid Mechanics* 971 (2023), A23. DOI: 10.1017/jfm.2023.636.

[Kár30] Theodore von Kármán. "Mechanische Ähnlichkeit und Turbulenz". In: *Nachrichten von der Gesellschaft der Wissenschaften zu Göttingen, Mathematisch-Physikalische Klasse* (1930), pp. 58–76.

[KKG18] Snehasis Kundu, Manotosh Kumbhakar, and Koeli Ghoshal. "Reinvestigation on Mixing Length in an Open Channel Turbulent Flow". In: *Acta Geophysica* 66.1 (2018). DOI: 10.1007/s11600-017-0109-7.

[KU14] Aman G. Kidanemariam and Markus Uhlmann. "Interface-resolved direct numerical simulation of the erosion of a sediment bed sheared by laminar channel flow". In: *International Journal of Multiphase Flow* 67 (Dec. 2014), pp. 174–188. ISSN: 0301-9322. DOI: 10.1016/j.ijmultiphaseflow.2014.08.008. URL: http://dx.doi.org/10.1016/j.ijmultiphaseflow.2014.08.008.

[LPR09] Victor S. L'vov, Itamar Procaccia, and Oleksii Rudenko. "Velocity and Energy Profiles in Two- vs. Three-Dimensional Channels: Effects of Inverse vs. Direct Energy Cascade". In: (2009). arXiv preprint. arXiv: 0902.2715 [physics.flu-dyn]. URL: https://arxiv.org/abs/0902.2715.

[LW18] Vincent Legat and Grégoire Winckelmans. *MéCANIQUE DES FLUIDES ET TRANSFERTS 1 (Notes pour le cours MECA1321)*. Lecture notes. Université catholique de Louvain. 2018.

[Mie10] S. A. Miedema. "Constructing the Shields Curve: A New Theoretical Approach and Its Applications". In: *Proceedings of the 19th World Dredging Congress (WODCON XIX)*. Ed. by J. Dobson. Beijing, China, 2010. URL: https://research.tudelft.nl/en/publications/constructing-the-shields-curve-a-new-theoretical-approach-and-its.

[Mie12] S. A. Miedema. "Constructing the Shields Curve Part A: Fundamentals of the Sliding, Rolling and Lifting Mechanisms for the Entrainment of Particles". In: *Journal of Dredging Engineering* 12.1 (2012), pp. 1–49. ISSN: 2150-9409. URL: https://research.tudelft.nl/en/publications/constructing-the-shields-curve-part-a-fundamentals-of-the-sliding.

[MM48] Eugen Meyer-Peter and Rolf Müller. "Formulas for Bed-Load Transport". In: *Proceedings of the 2nd Meeting of the International Association for Hydraulic Research*. IAHR. Stockholm, Sweden, 1948, pp. 39–64.

[NR86] Iehisa Nezu and Wolfgang Rodi. "Open-channel flow measurements with a Laser Doppler Anemometer". In: *Journal of Hydraulic Engineering* 112.5 (May 1986), pp. 335–355.

[OAG09] Malika Ouriemi, Pascale Aussillous, and Élisabeth Guazzelli. "Sediment dynamics. Part 1. Bed-load transport by laminar shearing flows". In: *Journal of Fluid Mechanics* 636 (2009), pp. 295–319. DOI: 10.1017/S0022112009007915.

[Our07] Malika Ouriemi. "Erosion, transport et instabilités d'un lit de particules dans un tube". French. PhD thesis. Université de Provence – Aix-Marseille I, 2007. URL: https://tel.archives-ouvertes.fr/tel-00202496.

[Pir14] Sergio Pirozzoli. “Revisiting the mixing-length hypothesis in the outer part of turbulent wall layers: Mean flow and wall friction”. In: *Journal of Fluid Mechanics* 745 (2014), pp. 378–397. DOI: 10.1017/jfm.2014.101.

[Pop00] Stephen B. Pope. *Turbulent Flows*. Cambridge: Cambridge University Press, 2000.

[Pra26] Ludwig Prandtl. *Turbulent Flow*. Tech. rep. 435. Translated from ”Über die ausgebildete Turbulenz”, ZAMM, 1926. NACA Technical Memorandum, 1926.

[Pra33] Ludwig Prandtl. *Recent Results of Turbulence Research*. Tech. rep. 720. Translation of ”Neuere Ergebnisse der Turbulenzforschung”, 1933. NACA Technical Memorandum, 1933.

[RA22] G. Rousseau and C. Ancey. “An experimental investigation of turbulent free-surface flows over a steep permeable bed”. In: *Journal of Fluid Mechanics* 941 (2022), A51. DOI: 10.1017/jfm.2022.310.

[RC13] T. Revil-Baudard and J. Chauchat. “A two-phase model for sheet flow regime based on dense granular flow rheology”. In: *Journal of Geophysical Research: Oceans* 118.2 (2013), pp. 619–634. DOI: 10.1029/2012JC008306. URL: https://doi.org/10.1029/2012JC008306.

[Rev+15] Thibaud Revil-Baudard et al. “Investigation of sheet-flow processes based on novel acoustic high-resolution velocity and concentration measurements”. In: *Journal of Fluid Mechanics Digital Archive* 767 (2015), pp. 1–30. DOI: 10.1017/jfm.2015.23. URL: https://hal.science/hal-01122373.

[Rev+16] Thibaud Revil-Baudard et al. “Turbulence modifications induced by the bed mobility in intense sediment-laden flows”. In: *Journal of Fluid Mechanics* 808 (2016), pp. 469–484. DOI: 10.1017/jfm.2016.671. URL: https://hal.science/hal-01660542.

[Rev14] Thibaud Revil-Baudard. “Experimental study and modelling of the sediment transport in sheet-flow regime”. Theses. Université de Grenoble, Nov. 2014. URL: https://theses.hal.science/tel-01122234.

[Ric59] F. J. Richards. “A Flexible Growth Function for Empirical Use”. In: *Journal of Experimental Botany* 10.2 (1959), pp. 290–300. DOI: 10.1093/jxb/10.2.290.

[Sch68] Hermann Schlichting. *Boundary–Layer Theory*. 6th ed. New York: McGraw–Hill, 1968.

[Shi36] Albert Shields. *Application of Similarity Principles and Turbulence Research to Bed-Load Movement*. Tech. rep. English translation by W. P. Ott and J. C. van Uchelen of the 1936 thesis. California Institute of Technology, 1936. URL: https://repository.tudelft.nl/record/uuid:a66ea380-ffa3-449b-b59f-38a35b2c6658.

[Sou06a] John Southard. *Introduction to Fluid Motions, Sediment Transport, and Current-Generated Sedimentary Structures*. MIT OpenCourseWare. 2006. URL: https://ocw.mit.edu/courses/12-090-introduction-to-fluid-motions-sediment-transport-and-current-generated-sedimentary-structures-fall-2006/ (visited on 08/12/2025).

[Sou06b] John B. Southard. *Introduction to Fluid Motions and Sediment Transport*. MIT OpenCourseWare Textbook. 2006.

[Van56] E. R. Van Driest. "On turbulent flow near a wall". In: *Journal of the Aeronautical Sciences* 23.11 (1956), pp. 1007–1011.

[VGI17] J. J. Voermans, M. Ghisalberti, and G. N. Ivey. "The variation of flow and turbulence across the sediment–water interface". In: *Journal of Fluid Mechanics* 824 (2017), pp. 413–437. DOI: 10.1017/jfm.2017.362.

[Vow+21] B. Vowinckel et al. "Rheology of mobile sediment beds sheared by viscous, pressure-driven flows". In: *Journal of Fluid Mechanics* 921 (2021), A20. DOI: 10.1017/jfm.2021.457.

[Yal77] M. Selim Yalin. *Mechanics of Sediment Transport*. 2nd ed. Oxford: Pergamon Press, 1977.

[YCH22] J. Yao, X. Chen, and F. Hussain. "Direct numerical simulation of turbulent open channel flows at moderately high Reynolds numbers". In: *Journal of Fluid Mechanics* 953 (2022), A19. DOI: 10.1017/jfm.2022.942.

UNIVERSITÉ CATHOLIQUE DE LOUVAIN
École polytechnique de Louvain
Rue Archimède, 1 bte L6.11.01, 1348 Louvain-la-Neuve, Belgique | **www.uclouvain.be/epl**